AMERICAN UNIVERSITY OF BEIRUT

CRYSTALLINE AND OPTICAL PROPERTIES OF ZINC OXIDE NANOPARTICLES SYNTHESIZED BY A SOLVENT BASED TECHNIQUE

by

REHAM ISSAM ABU AMER

A thesis
submitted in partial fulfillment of the requirements
for the degree of Master of Science
to the Department of Physics
of the Faculty of Arts and Sciences
at the American University of Beirut

Beirut, Lebanon
February 2015

AMERICAN UNIVERSITY OF BEIRUT

CRYSTALLINE AND OPTICAL PROPERTIES OF ZINC OXIDE NANOPARTICLES SYNTHESIZED BY A SOLVENT BASED TECHNIQUE

by

REHAM ISSAM ABU AMER

Approved by:

Dr. Malek Tabbal, Professor — Advisor
Department of Physics

Dr. Michel Kazan, Assistant Professor — Committee Member
Department of Physics

Dr. Charbel Madi, Visiting Assistant Professor — Committee Member
Department of Physics

Date of thesis defense: February 5, 2015

AMERICAN UNIVERSITY OF BEIRUT

THESIS, DISSERTATION, PROJECT RELEASE FORM

Student Name: Abu Amer (Last) Reham (First) Issam (Middle)

⊗ Master's Thesis ○ Master's Project ○ Doctoral Dissertation

[X] I authorize the American University of Beirut to: (a) reproduce hard or electronic copies of my thesis, dissertation, or project; (b) include such copies in the archives and digital repositories of the University; and (c) make freely available such copies to third parties for research or educational purposes.

[ ] I authorize the American University of Beirut, **three years after the date of submitting my thesis, dissertation, or project,** to: (a) reproduce hard or electronic copies of it; (b) include such copies in the archives and digital repositories of the University; and (c) make freely available such copies to third parties for research or educational purposes.

Reham February 5, 2015

Signature Date

This form is signed when submitting the thesis, dissertation, or project to the University Libraries

ACKNOWLEDGEMENTS

It is a pleasure to thank and offer my deep regards to all of those who supported me during the completion of this project.

First and foremost I offer my sincerest gratitude to my advisor, Prof. Malek Tabbal, for his invaluable guidance, support and continuous advice thoughout my dissertation research. His vision and methodological approach have been fundamental in shaping and writing this thesis. I am also sincerely grateful to Prof. Michel Kazan for his willigness to help as well as all the time he had spent teaching, guiding and encouraging me throughout my thesis. I appreciate his constant advice and kind patience, and I greatly benefited from his keen scientific insight and his vast knowledge in the field. My sincere thanks also goes to Prof. Charbel Madi for his invaluable comments and enlightening discussions to improve this work.

Special thanks to Prof. Digambara Patra, Associate Professor of Chemistry at AUB, for supporting us and allowing us to use his lab and materials to prepare our samples. I also owe a debt of gratitude to the helpful graduate students in his lab for their kind assistance.

Sincere thanks to the Central Research Science laboratory (CRSL) crew at AUB especially Joan Younes and Rania Shatila for the great help at all times.

I would also like to thank my colleagues for their support, assistance and emotional encouragement throughout my study here at AUB.

Finally, but not least, my sincerest love and deepest gratitude go to my family especially my parents for their endless love and emotional support. I am forever thankful for their constant support and hard work since the day that I was born. Without their words of encouragement, it would have been impossible to complete this work.

AN ABSTRACT OF THE THESIS OF

Reham Issam Abu Amer for Master of Science
Major: Physics

Title: Crystalline and optical properties of Zinc Oxide nanoparticles synthesized by a solvent based technique

ZnO nanoparticles were successfully synthesized via simple precipitation method by controlling different parameters of the precipitation process such as solution concentration and calcination temperature. The structural and morphological properties of these samples were investigated by SEM and XRD analysis. SEM images showed uniformity in the particles size and shape for ZnO nanoparticles calcined at different temperatures compared to the other synthesized samples. The average crystallite size increases with increasing the calcination temperature. We used UV-VIS and FTIR spectrophotometers to get the reflectivity data of the selected samples. By using Kramers-Kronig (K-K) method, we then determined the optical constants, n and k with the real and imaginary parts of the dielectric constant in the IR region. The K-K method was then combined with a newly developed technique to compute the optical parameters in the UV-VIS region. A shift in the absorption peak in the extinction coefficients of the samples was observed due to defects by varying the calcination temperature. Green emission was observed from 36 nm grain size ZnO samples and yellow emission was observed from 470 nm grain size ZnO samples. Finally, to verify the validity of our approach, we back calculated the UV-VIS reflectivity spectra from the deduced optical parameters, and good agreement was found between the measured and calculated spectra. This confirms the importance of our approach in developing a new numerical technique for accurate measurement of the optical parameters at the UV-VIS wavelengths. The reflectivity based technique described in this work could be applied to study ZnO nanoparticles of smaller sizes reaching the quantum confinement region.

CONTENTS

CHAPTER I

INTRODUCTION

A. Zinc Oxide: Properties and Applications

Zinc oxide (ZnO) is a II-VI semiconductor known for its versatile applications in nano-scale electronic and optoelectonic devices [1]. It crystallizes in three forms: hexagonal wurtzite, cubic zincblende, and cubic rocksalt structure. The wurtzite structure is most stable and thus most common at ambient conditions. The zinc blende form can be stabilized by growing ZnO on substrates with cubic lattice structure. The rocksalt structure is stable only under high pressure about 10 GPa [2]. In the ZnO wurtzite structure the lattice parameters are a=3.25 Å and c=5.2 Å. It is characterized by tetrahedral coordination where each zinc ion is surrounded by a tetrahedron of oxygen ions, and vice versa as shown in Figure 1.

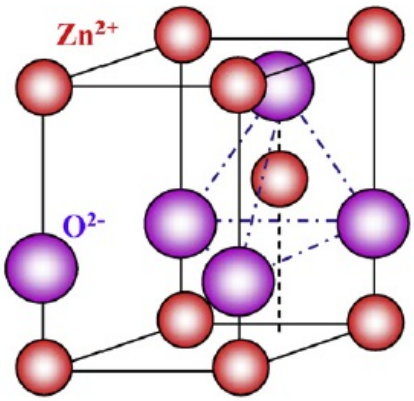

Figure 1: Schematic diagram of ZnO wurtzite structure [3]

The tetrahedral coordination of wurtzite ZnO gives rise to non-centrosymmetric structure and consequently piezoelectricity and pyroelectricity. ZnO has the largest piezoelectric response of any tetrahedrally bonded semiconductor where it finds broad appli-

cations in piezoelectric devices such as surface acoustic wave (SAW) resonators, sensors and filters, and micro- and nano- electromechanical systems (MEMS and NEMS) [4].

ZnO is a direct wide bandgap semiconductor of 3.37 eV at room temperature. This enables applications in short wavelength optoelectronic devices such as ultraviolet or blue light emitting diodes, laser diodes, and photodetectors [4]. ZnO has great advantages for optoelectronic applications over the currently used wide bandgap compounds such as SiC and GaN. The most important advantage is the high exciton binding energy (60 meV) giving rise to efficient exitonic emission at room temperature and even at higher temperatures [1]. The large exciton binding energy makes ZnO a promising material for optical devices that are based on excitonic effects. It paves the way for laser operation based on excitonic transitions [4]. Besides, ZnO has high transparency to visible light, which enables transparent electronic applications such as flat panel displays and solar cells. Table 1 gives a comparison of ZnO material properties with other wide bandgap semiconductors [1].

Table 1: Comparison of ZnO Properties with Other Wide Bandgap Semiconsuctors

Material	Crystal Structure	Bandgap (eV)	Lattice a (Å)	Constant c (Å)	Exciton Binding Energy (meV)
ZnO	Wurtzite	3.37	3.25	5.21	60
ZnS	Wurtzite	3.68	3.82	6.26	39
ZnSe	Zinc blende	2.7	5.67	-	20
GaN	Wurtzite	3.4	3.19	5.19	21
6H-SiC	Wurtzite	2.9	3.08	15.1	-

Room temperature photoluminescence spectrum of ZnO shows two main bands; UV emission band at $\sim$ 380 nm and a broad emission band in the green spectral range at $\sim$ 530 nm. The UV emission band is commonly attributed to the near band edge transi-

tion of ZnO, namely the free excitons recombination. Whereas the broad emission band has been attributed to several defects in the crystal structure such as O-vacancy [5], Zn-vacancy [6], O-interstitial [7] and Zn-interstitial [5].

ZnO has high breakdown electric field of $\sim 2 \times 10^6\ V/cm$ where high operation voltage could be applied to ZnO-based devices. It has large saturation velocity of 3.2 $\times\ 10^7\ cm/sec$ at room temperature making ZnO-based devices better for high frequency applications. Its melting temperature is $\sim$ 2000 °C providing the ability to function under high operating temperature [8].

ZnO is intrinsically an n-type semiconductor due to defects such as oxygen vacancies and zinc interstitials. The major challenge for widespread exploitation of ZnO in electronic and photonic applications is the difficulty in p-type doping. P-type doped ZnO is unstable and reverts to n-type state within a very short period of time [9]. The ability to achieve p-type doping in ZnO is of great interest for the fabrication of p-n junction from them for device applications such as diode lasers and UV light emitting diodes [10].

The intrinsic carrier concentration of ZnO is typically at the level of $10^{16}\ /cm^3$. The electron Hall mobility in ZnO single crystals is of the order of 200 cm^2/V.s at room temperature. Due to the relatively high electron mobility, ZnO hold advantages over other wide band gap materials such as TiO_2 in photo-electro-chemical applications, such as photocatalysis and dye sensitized solar cell [11].

ZnO has relatively high heat capacity, high heat conductivity and low thermal expansion. The specific heat capacity of ZnO is reported to be about 40 J.mol^{-1}K^{-1} at 300 K [12]. The thermal expansion coefficients are reported as a_c = 2.49 $\times\ 10^{-6}$ K^{-1} and a_a = 4.31 $\times\ 10^{-6}$ K^{-1} for expansion parallel and perpendicular to c-axis respectively

[13]. The thermal conductivity of ZnO is reported to be about k = 1.0 W cm^{-1} K^{-1} at 300 K, making ZnO suitable material for high power electronic devices [14].

Besides, ZnO is very resistive to high energy radiation, making it a suitable candidate for space applications than other wide bandgap semiconductors [8]. It is also considered as one of the most widely used gas sensing material where it has great potential in sensing various gases such as CO, H_2, NH_3 and ethanol [15].

ZnO is a versatile functional material and promising for multifunctional applications in nanoscale electronic and optoelectronic devices. It is thus essential to know the optical constants of ZnO for accurate modeling and design of optoelectronic devices. Since the specific properties of ZnO and its applications are mainly depending on their structure, size and morphology, many researchers explored various methods of synthesis of ZnO nanomaterials in different sizes and structures, such as nanocombs, nanorings, nanohelixes, nanosprings, nanobelts, nanowires and nanocages [16]. From here stems our interest to investigate the crystalline and optical properties of ZnO nanoparticles synthesized by a simple precipitation method. The synthesis was done by controlling different parameters of the precipitation process such as solution concentration and temperature. The structural and optical properties of the prepared samples were investigated by X-ray diffraction (XRD), Scanning Electron Microscopy (SEM), UV-VIS reflectance, and FT-IR reflectance. The optical constants such as dielectric function, refractive index, n, and extinction coefficient, k, were determined for ZnO nanoparticles having different sizes over a wide spectral range in the UV-VIS-NIR as well as in the mid-infrared region.

B. Thesis Organization

The structure of the thesis is organized as follows. After this introduction (chapter 1), the second chapter presents an overview on the optical studies done on ZnO and the experimental methods that were used to extract the optical parameters. The third chapter presents a thorough explanation of the experimental aspect of the work and explains our newly developed code that is used in combination with the Kramers Kronig method to extract the optical properties of our samples. The fourth chapter presents the experimental results of our work followed by a physical interpretation of the obtained results. The last chapter provides a summary of our work with some perspectives for future work in the field.

CHAPTER II

LITERATURE REVIEW

In this chapter, an overview of the optical studies completed on ZnO is presented.

Several studies have been done to analyze the optical properties of ZnO and the field is still wide open due to its potential in device application. The optical parameters of ZnO such as refractive index, n, extinction coefficient, k, and dielectric constant ε have been reported by several authors using different methods. Refractive index dispersion of ZnO single crystal has been initially reported by Mollwo [17] and Bond [18] using the method of minimum deviation in the visible and near infrared region at room temperature. Park and Schiender [19] then extended the measurements from room temperature down to liquid-helium temperature and the region near the absorption edge for both ordinary ($E \perp c$) and extraordinary ($E \| c$) refractive indices using transmission interferometry. It was found that the dispersion curves at room temperature are similar to those reported by Mollwo [17], but they were extended to include the optical isotropic point. However, by lowering the temperature, the dispersion curves were observed to get sharper and become blue shifted.

Hengehold et al. [20] studied the optical anisotropy of ZnO beyond the fundamental absorption edge using unpolarized light. The reflectivity of ZnO platelets was measured over an energy range of band gap to 22 eV. From reflectivity, a dispersion analysis was done to determine the optical constants n and k, and the complex dielectric function ε. A comparison of the energy loss function obtained from the ultraviolet-reflectivity spectrum with that from the electron-transmission measurements has been carried out and good agreement was found. A similar study was done by Klucker et al. [21] using linearly

polarized light. The reflectivity of ZnO single crystals was measured at near normal incidence in the energy region from 3 to 25 eV with light polarized parallel and perpendicular to the c-axis. The real and imaginary parts of the complex dielectric function $\varepsilon = \varepsilon_1 + i\varepsilon_2$ as well as the energy loss function $L = |\mathrm{Im}\ \varepsilon^{-1}|$ have been computed from the reflectivity data by means of Kramers-Kronig analysis for both directions of polarization.

Hu et al. [22] measured the optical functions of ZnO thin films in the wavelength range 350 - 900 nm. The refractive indices were calculated from the transmittance oscillations, fitted to the Cauchy's equation, and were found to be 0.02 - 0.03 lower than that of the bulk crystal reported by Bond [18]. The existence of grain boundaries in the films was attributed to be the source for this difference. Using the prism-film coupling method, the optical waveguide properties were measured and waveguide equations that suit the anisotropic waveguide structures were derived to determine the ordinary n_0 and extraordinary n_e refractive indices. The values of the indices were found to be n_0 =1.96 and n_e = 1.98 which were much closer to that of bulk crystal. Measurements of the optical parameters of ZnO thin film in the same spectral range have been also reported by Sun et al. [23] using variable angle spectroscopic ellipsometry (VASE). The refractive index, n, and the extinction coefficient, k, were extracted by fitting the measured VASE data (ψ, Δ) by the Sellmeier equation.

Measurements of the complex dielectric functions ε(E) of ZnO were reported by Yoshikawa and Adachi [24] using spectroscopic ellipsometry in the photon energy range of 1.5 - 5.0 eV at room temperature.The measured ε(E) spectra were analyzed on the basis of a simplified model of the interband transitions and good agreement was found between the calculated and experimental results. The optical constants related to dielectric function such as complex refractive index, absorption coefficient and normal incidence reflectivity have been also determined. The data for polarization parallel (E||c) and perpendicular

(E⊥c) to the optical axis agreed very well with Bond's bulk refractive index data.

A two modulator generalized ellipsometry (2-MGE) technique was used by Jellison and Boatner [25] to determine the anisotropic optical functions of uniaxial ZnO. This technique was claimed to produce the most accurate results of the optical functions of ZnO above the direct band edge, particularly in the spectral region of 3.3 - 5.0 eV. The refractive indices determined below the direct band edge were observed to show good agreement with the minimum-deviation method. The spectrum of the optical dielectric response functions showed one isotropic point at 3.114 eV, and a near-isotropic point near 3.31 - 3.34 eV.

Ashkenov et al. [26] reported the infrared dielectric functions and phonon modes of bulk and thin film ZnO samples using infrared (300 - 1200 cm^{-1}) spectroscopic ellipsometry and Raman scattering measurments. The film ZnO phonon mode frequencies was found to be highly consistent with those of the bulk sample. A small redshift was observed in the film longitudinal optical (LO) phonon mode frequencies which has been attributed to the existence of vacancy point defects within the films. The static dielectric constant ε_0 was obtained from infrared spectroscopic ellipsometry measurements, and the high-frequency dielectric constant ε_∞ was calculated through the Lyddane-Sachs-Teller (LST) relation using the static constant and the TO- and LO-phonon mode frequencies. The results were compared with some previously reported data obtained from different measurement methods as shown in Table 2.

Şenadım et al. [27] used different methods to investigate the optical parameters of ZnO thin film in the ultraviolet-visible-near infrared regions (190 - 1100 nm). Kramers-Kronig analysis and the envelope method were employed to determine the refractive index, n, as a function of wavelength. The data obtained from the envelope method were

Table 2: Static and high frequency dielectric constants of ZnO [26].

Sample		Ashkenov et al. [26]		Yoshikawa and Adachi [24]	Bond [18]
		Thin	film Bulk	Bulk	Bulk
ε_0	E⊥c	7.46	7.77	7.61	7.65
	E‖c	8.59	8.91	8.50	8.57
ε_∞	E⊥c	3.61	3.70	3.68	3.70
	E‖c	3.76	3.78	3.72	3.75

consistent with Kramers-Kronig relation results. The complex dielectric constant and dispersion energy were calculated using Kramers-Kronig and dispersion relations. The energy band gap was determined from the spectra of the real dielectric coefficients and good agreement was found with the experimental value which was 3.22 eV. The refractive index dispersion in the transparent region was analyzed using the single oscillator model.

Xue et al. [28] investigated the effects of the annealing temperature on the optical properties of ZnO thin film annealed at different temperatures ranging from 600 °C to 950 °C using transmittance spectrum. The optical absorption edge was observed to be blue shifted when the annealing temperature decreases below 750 °C while red shifted when the annealing temperature exceeds 750 °C. The blueshift and redshift has been attributed to the improvement and degradation of the quality of the ZnO thin film respectively. With increasing the annealing temperature, they found that the optical constants decrease in the ultraviolet region while increase in the visible region.

Characterization of far-infrared optical properties of bulk and nanostructured ZnO has been carried out by Han et al. [29] using non-polarized radiation. The measurements were done using THz time-domain spectroscopy in the frequency range extending from 0.3 to 3.5 THz. The measured data of power absorption and refractive index allow the calculation of the real and imaginary parts of complex dielectric function. Theoretical

calculations were done to investigate these parameters based on dielectric models combined with the effective medium theories. The experimental data was compared with the theoretical fitting and good agreement was found.

Based on theoretical models, Schleif et al. [30] computed the dielectric function, the reflectivity, and the electron-energy-loss function of wurtzite ZnO using many-body ab initio calculations over a wide spectral range of photon energy up to 32.5 eV. The macroscopic dielectric function $\varepsilon(\omega)$ was obtained by solving the Bethe-Salpeter equation (BSE) including excitonic and loca-field effects (LFEs). The precised computation for the real and imaginary parts of $\varepsilon(\omega)$ allows the derivation of reflectivity as well as the electron-energy-loss function spectra. The calculated dielectric functions were compared with the experimental findings and convincing agreement was found.

Caglar et al. [31] investigated the influence of In doping on the optical constants of ZnO films in the wavelength range 300-800 nm. The refractive index, n, and the extinction coefficient, k, were determined using transmittance and reflectance spectra. The calculated values of n and k allows the computation of the real and imaginary parts of the dielectric constant ε. The value of the direct band gap Eg was observed to decrease with increasing doping concentration, whereas the optical parameters of the films tend to increase with In doping. It was found that the dispersion parameters of the films obeyed the single oscillator model.

Using polarized far-infrared (FIR) reflectance technique, Abrishami et al. [32] studied the optical properties of pure and Mn doped ZnO nanoparticles. Optical characterization were carried out using Fourier transform infrared spectroscopy (FTIR) in the range of 400-2000 cm^{-1}. Kramers- Kronig analysis was employed to evaluate the optical constants i.e. refractive index (n) and dielectric constants (ε). The values of the optical

constant n and ε were reported in the range between 1 to 7 and -25 to 35, respectively. It was shown that the dielectric constant ε and the ratio of longitudinal (LO) to transverse (TO) optical mode frequency increased with increasing the doping level of Mn. Comparison of dielectric function between bulk and nanopowders of ZnO samples showed a broadening in the real part ε_1(w) as a consequence of particles size effect.

Similarly, Pohkok et al. [33] used polarized far infrared reflectance technique to determine more informative and accurate results of ZnO material parameters than that obtained with non-polarized measurements. The authors demonstrated experimental and theoretical results of the s- and the p-polarized FIR reflectivity spectra at various angles of incidence, from 20° to 70°, for wurtzite single crystal ZnO. The theoretical measurement were stimulated based on anisotropic dielectric function model, and good agreement was found with the experimental one. Additionally, FIR optical properties such as the complex dielectric function, the refractive index, the absorption coefficient and the reciprocal of the absorption coefficient have been also obtained through numerical calculation.

Serbetçi et al. [34] investigated the optical and dispersion energy parameters of nanostructure ZnO film in the ultraviolet-visible-near infrared region. The diffuse reflectance, transmittance, and absorbance spectra of the ZnO film were measured using UV-VIS-NIR spectrophotometer attached an integrating sphere.The refractive index of the film was analyzed by two methods; single oscillator model and single oscillator Forouhi-Bloomer model from which the dispersion energy E_d and oscillator energy E_0 were calculated. Phan et al. [35] investigated the effect Ga-doping on the optical properties of ZnO nanostructure films in UV-VIS-NIR region. The absorption coefficient α, computed from the experimental measurements of the transmittance T (λ) and reflectance R (λ) spectra, contributed to the determination of the refractiive index n as well as the real and imaginary parts of the dielectric constant ε. It was found that the optical parameters

of the film affected by the Ga doping concentration. We also mention the work of Ilican [36] who was concerned with the effect of Na doping on the optical properties of ZnO nanorod. He found that the optical band gap decreases with increasing Na concentration. The optical constants were determined using transmittance and reflectance spectra in the wavelength range 300-800 nm. Enhancement in the optical constants was observed by increasing the concentration of Na doping, and the dispersion parameters was found to obey the single oscillator model.

Multiple oscillator models were used by Khoshman et al. [37] to investigate the optical constants of polycrystalline ZnO thin films over a wide spectral range. The thickness and the optical constants of the ZnO thin films were determined using variable angle spectroscopic ellipsometry (VASE) through multiple oscillator models in the ultraviolet-visible-near infrared range (190-1400 nm). A linear combination of "Psemi-M0" model and multiple Gaussian models were employed to fit the optical constants of the ZnO thin film, while simultaneously enforcing Kramers-Kronig consistency in the fitted ellipsometric parameters. The refractive indices of the films were reported to be in the range from 1.68 to 1.93 and the extinction coefficients in the range from 4.56×10^{-6} to 0.23.

Recently, the Kramers-Kronig (K-K) method and classical dispersion theory were used by Zamiri, Reza, et al. [38] to study the far infrared optical constants such as, refractive index $n(\omega)$, dielectric constant $\varepsilon(\omega)$, transverse optical phonon (TO) and longitudinal optical phonon (LO) modes for ZnO and ZnO/Ag nanoplates. An abrupt change in the reflectance spectra was observed at a wavelength around 385 nm in both samples, which has been attributed to the recombination of electron holes in ZnO. Strong peaks were observed for $n(\omega)$ and $k(\omega)$ at around 415 cm^{-1} and 410 cm^{-1} , respectively. The intensity of the peaks were found to be n_{max} = 8.80 and k_{max} = 4.16 for ZnO nanostructures. However, enhancement in the optical constants was observed when Ag was

deposited on the surface of ZnO nanoplates. The intensity of the peaks were found to be 28.80 and 13.30 for $n(\omega)$ and $k(\omega)$ respectively.

All the methods mentioned so far, have a certain limitation in their precision or functional range to characterize the optical properties of a sample. Fo rexample, spectroscopic ellipsometry and the first principle methods are only applicable for highly purified samples. On the other hand, the envelope method can only be used in a frequency region where substrate absorption is quite small. Furthermore, Kramers Kronig analysis of the reflectivity spectra requires reflectivity data from zero to infinite frequencies, so low- and high-frequency extrapolations for reflectivity spectrum should be used. Such extrapolations can be predictable in the IR region where a constant reflectivity tail at the lowest as well at the highest frequencies can be used. However, in the UV-VIS region, we are unable to predict the shape of the reflectivity spectra and consequently this can result in large phase error in the obtained optical data. Out of all these methods, the K-K analysis of the reflectivity spectra is still the most efficient technique when intrinsic and defect response are needed. Therefore, a new method is required to be combined with the Kramer Kronig analysis to improve the extrapolation part of the spectrum in the UV-VIS region into a reliable one.

In this thesis, we report our systematic efforts to combine the K-K analysis technique with our newly developed code to obtain the refractive index, the extinction coefficient and the dielectric constants in the UV-VIS region. The reflectivity model that we used is based on the equation of unpolarized reflectance derived from the behaviour of light at the interface between two media along with the K-K analysis technique. This approach was applied to our samples to extract their optical parameters and back calculation was done to check the validity of the code. A fully elaboration of our approach is presented in chapter 3.

CHAPTER III

EXPERIMENTAL TECHNIQUES

In this chapter, we will present the experimental methods that were used in this study, including the nanostructure synthesis process, the Scanning Electron Microscope (SEM) used for morphological characterizations and the X-Ray Diffractometer (XRD) used for structural analysis. We will also describe the UV-VIS-NIR and FTIR spectrometers used for reflectivity measurements along with the numerical techniques that were used to extract the optical paramters of our samples in both regions.

A. Samples preparation

ZnO nanoparticles were synthesized by a simple precipitation method in Prof. Patra's lab in the Chemistry Department at AUB. In this method zinc nitrate $(Zn(NO_3)_2 \cdot 6H_2O)$ and potassium hydroxide (KOH) were used as a starting materials. The synthesis was done by controlling different parameters of the precipitation process such as zinc nitrate concentration, potassium hydroxide concentration as well as the calcination temperature in order to establish the best parameters for which ZnO nanoparticles are obtained.

The first synthesis process was done using 0.1 M $Zn(NO_3)_2 \cdot 6H_2O$ and 0.2 M KOH prepared in 50 ml deionized water. The potassium hydroxide solution was added drop by drop into the zinc nitrate solution under vigorous stirring at 4 °C, and the stirring was continued overnight. The resulting precipitating solution was turned to whitish cloudy. The white precipitate product was collected by centrifugation at 4000 rpm for 30 min and washed thoroughly with deionized water to remove any impurities. The obtained product was then freeze dried and calcined in furnace oven at different temperatures: 300 °C, 500 °C, 700 °C, and 900 °C for 2 h.

The same synthesis process was followed by varying the concentration of the KOH solution and fixing the calcination temperatures at 500 °C. Concentrations of KOH solution of 0.1, 0.2, 0.3 and 0.4 M were used.

In the third precipitation process, the concentration of zinc nitrate was modified. The calcination temperature was also fixed at 500 °C and concentrations of zinc nitrate solution of 0.05, 0.1, 0.15 and 0.2 M were used.

B. Scanning Electron Microscope (SEM)

Scanning electron microscope is a powerful magnification tool used to produce images of a sample by scanning it with a focused electron beam. It provides information about the sample's surface topography, morphology and composition. The electron beam is scanned in a raster pattern over the sample's surface and the signals derive from electron-sample interactions are recorded by detectors to produce an image.

The experimental setup consists of an electron gun, column, sample chamber, detectors and vacuum chamber, and is represented in Figure 2.

Electron gun: It is based on thermal emission of electrons. By applying thermal energy to a filament, usually made of tungsten, electrons are emitted toward the specimen under examination.

Column: The column consists of two lenses made from magnets capable of bending the path of electrons. The first lens called condenser lens demagnify the beam into a small area called a spot, while the second called objective lens focuses the beam onto the sample. In the column, there is also a beam splitter called stigmator responsible to create a magnetic field around the beam to restore it in a circular cross section.

Sample chamber: It is the area where the specimen is placed. It must be sturdy and insulated from vibration in order to produce a clear image. The sample holder depend on

the size and shape of the sample, and the sample can be translated in three dimensions as well as rotated.

Detectors: Different detectors can be used depending on the type of information to be obtained from the sample. The most common one is the secondary electron detector (SE) used to provide information about the surface topography. Other detectors, such as backscattered electron detector and X-rays detector, provides information about the composition of the sample.

Vacuum chamber: SEM requires a vacuum to operate in order to keep the electron beam from constant interference with air particles in the atmosphere. The air particles are bad for the electron beam in that the particles would block its path toward the specimen or the electrons would be knocked out of the air and onto the specimen, which will distort the specimen's surface.

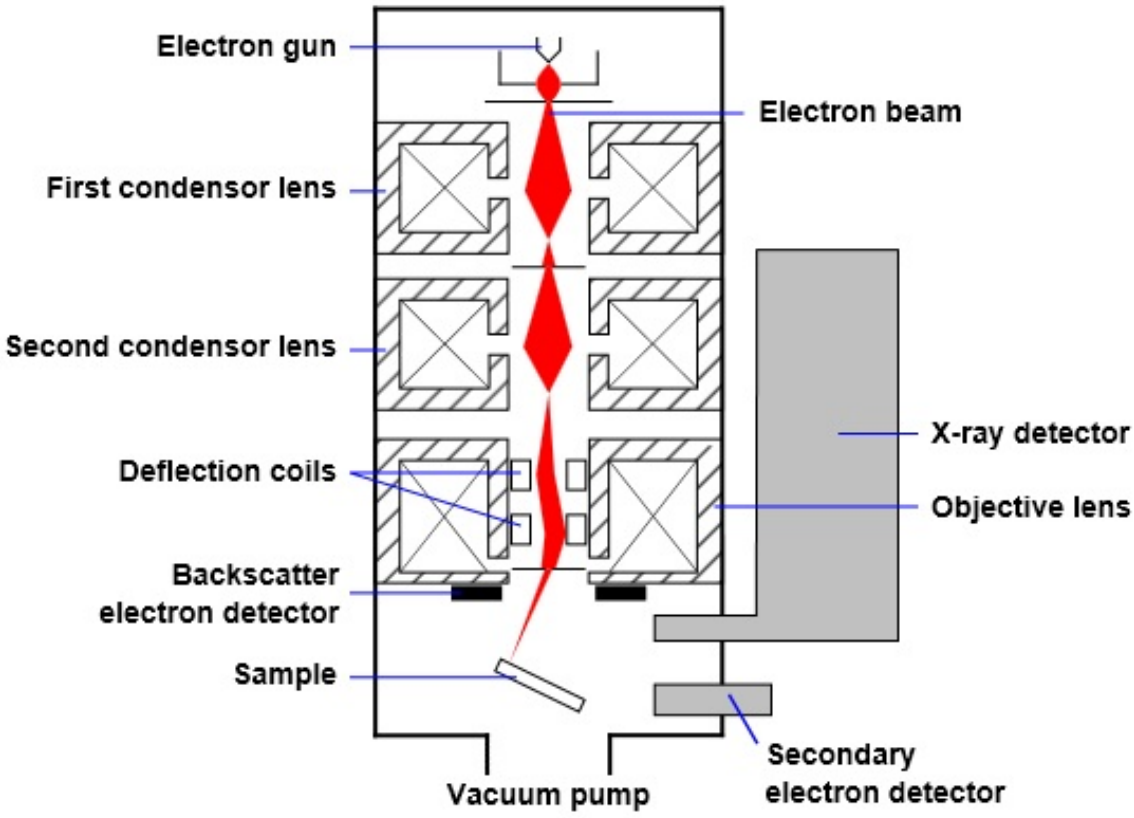

Figure 2: Optical diagram for scanning electron microscope[39]

In SEM, scanning coils are used to manipulate the electron beam. They create a magnetic field using fluctuating voltage so that they are able to move the beam precisely back and forth over the area of interest. The beam energy is typically in the range of 500 eV to 30 keV. Upon interaction with the specimen, electrons are emitted from the sample due to elastic and inelastic scattering events within the sample's surface and near-surface material. Low energy electrons resulting from inelastic scattering are emitted from the sample's surface with an energy in the range of 50 eV or less. These are known as secondary electrons and they are mostly used for the imaging of the sample's surface topography. High energy electrons are ejected due to elastic collision of the incident electron with the atomic nucleus, and they are called backscattered electrons. The energy of backscattered electrons is comparable to that of the incident electrons and their yield is related to the average atomic number of the sample's material. Hence, backscattered electron imaging provides image contrast as a function of elemental composition. X-ray characteristic can also be used to analyze the elemental composition and distribution within the sample. The interaction volume between the electron beam and the specimen with the various electrons emitted and their respective energies is shown in Figure 3.

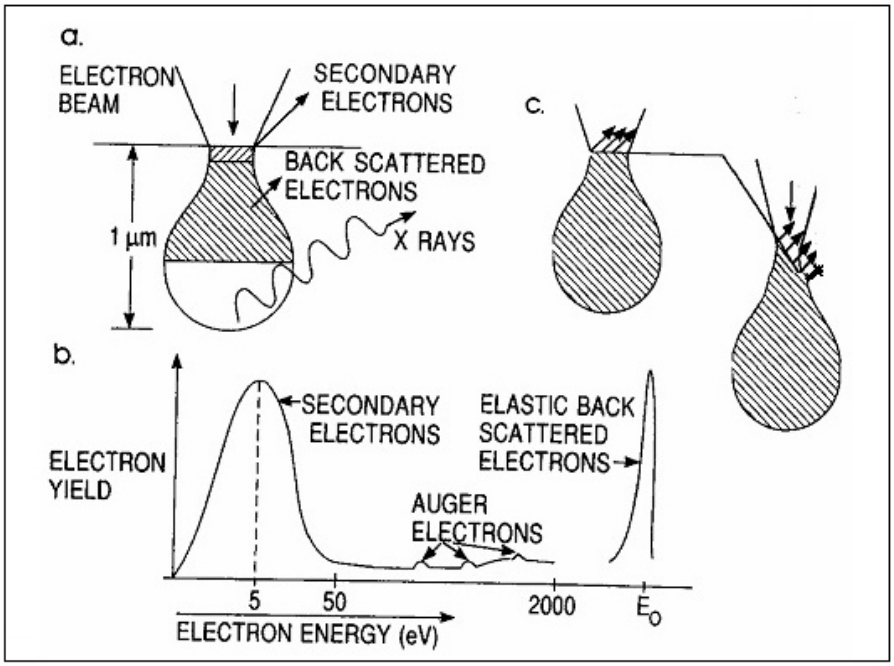

Figure 3: (a) Electron interactions with the surface during bombardment. (b) Type of electrons and corresponding energies of the emitted electrons after element interaction. (c) Effect of surface topography on electron emission.[40]

Characterization of the samples was done using a TESCAN MIRA3 scanning electron microscope. All samples were sputtered with a thin layer of gold (Au) to prevent charging of the specimens by the electron beam during the measurement and improve the signal and the quality of the images taken on the SEM. Detection of the secondary electrons was done using in-beam detector instead of SE detector. The in-beam detector is located in the objective lens where it attracts electrons emanating from the sample surface into the objective lens and catches them there. This allows the observation of specimens at very short working distances (WD) and thus improved resolution contrast to the SE detector which would not have a good signal at short WD because the path of secondary electrons from the specimen to the standard SE detector would be shielded by the column. Moreover, the combined electrostatic-magnetic lens gives further improvement of microscope performance.

C. X-Ray Diffraction

X-ray diffraction is a powerful non-destructive technique for characterizing crystalline materials. It provides information about the crystal structure, chemical composition, orientation of crystallites and other structural parameters such as lattice parameters and average grain size. It is based on constructive interference of monochromatic X-rays scattered at specific angles from the regular arrangement of atoms in the crystal. Consequently, the X-ray diffraction pattern acts as a fingerprint of the periodic atomic arrangement in a given material. The result is a plot of diffracted intensity against the angle of the detector, 2θ.

1. Physical Principles

a. Generation of X-rays

X-rays are produced when high energy electrons strikes with a metal target. They can be generated by an X-ray tube, a vacuum tube that usually consist of two electrodes; cathode and anode. When an electric current passes through the filament (cathode), it will heated up and starts emitting electrons. The electrons emitted are accelerated under the high voltage and directed toward the target metal (anode). When the electrons hit the target, X-rays are produced by two different atomic processes; X-ray fluorescence and Bremsstrahlung. X-ray fluorescence occurs when high energy electron knock an electron out of the inner shell of the target metal. An electron from a higher energy level will then transfer to fill the vacancy emitting X-rays with precise energies determined by the electron energy levels. These X-rays are shown at few discrete frequencies in the emission spectrum and called characteristic X-rays. However, Bremsstrahlung occurs when the high energy electrons are decelerated by the atomic nucleus of the target. In this case a continuous spectrum of X-rays is formed and the radiation produced called Bremsstrahlung radiation.

b. Bragg's Law

The X-ray waves emanating from a set of discrete parallel planes containig atoms arranged periodically in a crystal lattice structure are in phase and constructively interfere when the Bragg condition is met. This is described by the relation.

$$n\lambda = 2dsin\theta \tag{1}$$

where n is an integer, λ is the wavelength of the incident x-ray, d is the distance between atomic planes and θ is the angle between incident ray and the scatter plane. A schematic illustration of the requirements of Bragg's law is shown in Figure 4.

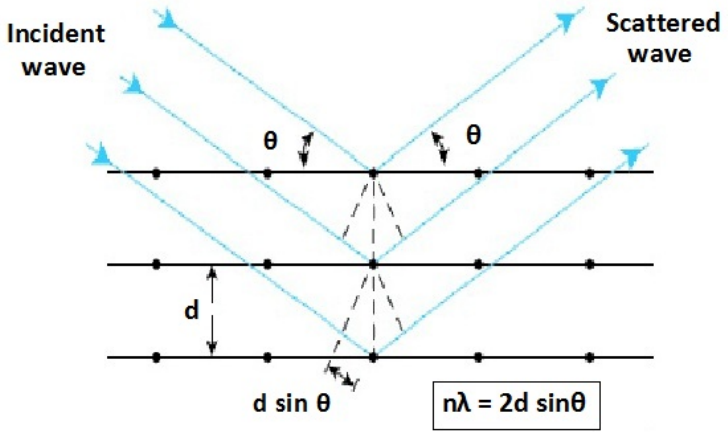

Figure 4: Schematic of Bragg's law condition.

2. Powder X-Ray Diffractometer

The structural and chemical analysis of our samples was done using the D8 ADVANCED X-ray diffractometer. It consists of an x-ray source, a sample holder and an x-ray detector. For the XRD analysis, fine powder sample is placed on the sample holder and the powder is assumed to consist of randomly oriented crystallites. The X-ray source

directs x-ray radiation at an angle θ toward the sample, while the detector located in the opposite side reads the intensity of the x-ray it receives at an angle 2θ away from the source path. The incident angle then increased over time while the detector angle always remains at an angle 2θ above the source path. A schematic diagram of the basic components of diffractometer is shown in the Figure 5. The X-ray radiation generated by an X-ray tube filtered by foils to produce monochromatic X-rays. The rays then pass through slits which collimate the X-ray beam. As the X-ray source and detector are rotated, the intensity of the reflected X-rays is recorded. When the geometry of the incident X-ray with sample satisfies Brag's law, constructive interference occur. This gives rise to a peak in the diffracted pattern. The detector record this X-ray signal and converts it to a count rate which is then displayed on the computer monitor as a function of the detector angle 2θ. For data interpretation and chemical analysis, the results were saved in a file and EVA software was used for evaluation.

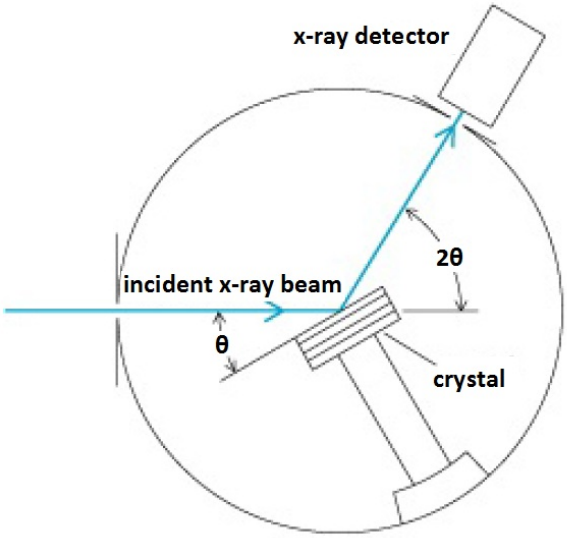

Figure 5: A simple representation of X-ray diffractometer.

D. Fourier Transform Infrared Reflectance and Analysis

Fourier Transform Infrared (FTIR) spectrometer is a powerful non-destructive analytic tool concerned primarily with molecular vibrations. The basic principle of this technique is infrared absorption at characteristic resonance frequencies of the material which correspond to the frequencies of vibrations between the bonds of the atoms making up the sample. Because each material is a unique combination of atoms, the infrared spectrum can be regarded as its fingerprint. The peaks in the IR specrtum of a sample represents the excitation of the vibrational modes of the molecules in the sample. A type of FTIR spectrometer measurements is the diffuse relection FTIR measurement that we have used in our research. By measuring the reflected light, the absorption properties of the sample can be extracted.

1. Experimental Setup

The FTIR setup that we used in our measurements is the Nicolet 4700 spectrometer from the Thermo Electron Corporation in the mid-infrared range 400-4000 cm^{-1}. The central component of this setup is a two-beam interferometer, an instrument that uses the technique of superimposing (interfering) two or more waves, to detect differences between them. To see how such a device operate, we can consider the effect of Michelson interferometer, one of the most commonly used devices, on a collimated beam of monochromatic radiation as shown in Figure 6.

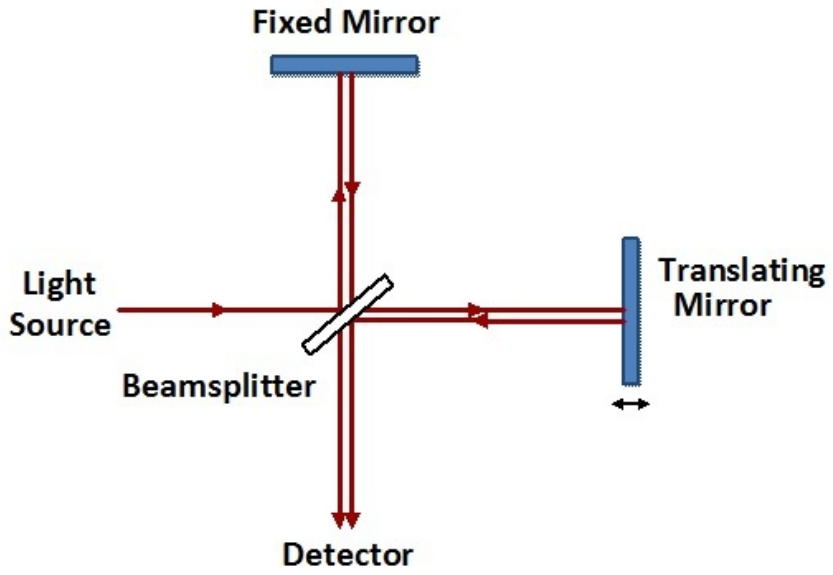

Figure 6: Schematic illustration of Michelson interferometer.

The Michelson interferometer consists of a beamsplitter and two perpendicularly plane mirror; one fixed and one movable. It uses the beamsplitter to split the radiation from the infrared source into two parts, one being reflected to the stationary mirror and the other part being transmitted to the movable mirror. When the two beams are reflected back, they recombine at the beamsplitter producing a constructive and destructive interference pattern due to the path diference between the two components of the beam.The intensity of the beam is calculated with respect to the optical path difference that is equal to double the displacement of the moving mirror. The interference pattern produced, the so-called an interferogram, continues its way and directed to the sample where energy absorption occurs at specific frequencies that are uniquely characteristic of the sample.

Since we are using powder samples which undergo diffuse reflection rather than specular one, we attached the Thermo Scientific Smart Diffuse Reflectance Accessory (DR) to measure the reflectivity spectrum. The DR device is highly effective at maximizing the diffusely scattered radiation while minimizing the specular reflected radiation which is a source of spectral inteference. It comes complete with two sample slides; one

holder has an integral sample cup and the second holder has an integral gold mirror that can be used as a background reference. This device operates by directing the IR beam from the interferometer, the interferogram signal, into the sample cup filled with the solid powder. The infrared radiation then interacts with the particles causing the light to diffuse or scatter as it moves throughout the sample. The output mirrors collect the diffusely scattered radiation which is directed to the detector in the spectrometer as shown in Figure 7.

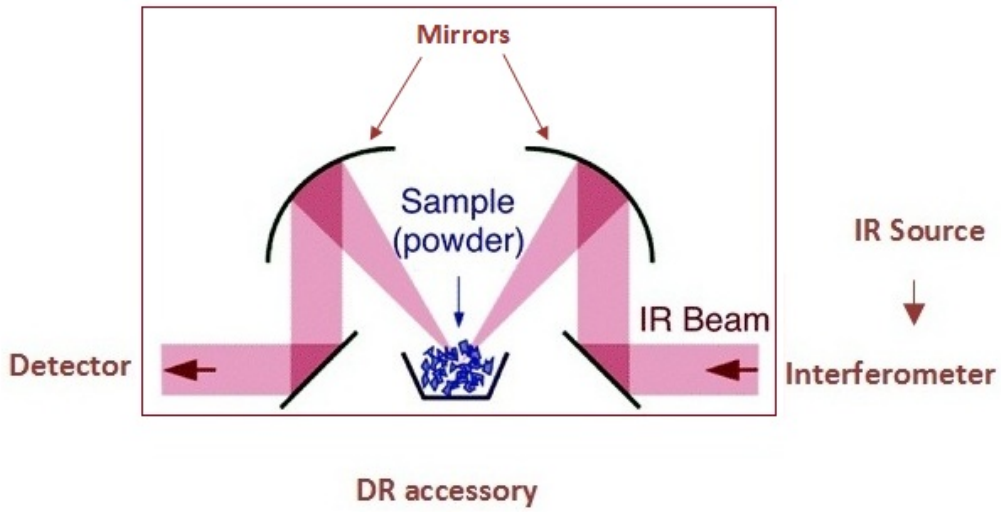

Figure 7: Diffuse reflectance FTIR spectrometer.

The resulting interferogram signal contain all the informaton required to produce the IR spectrum of the sample but in the time domain. In order to obtain interpretable information, the computer transforms the interferogram signal recorded by the detector into a frequency distribution spectrum (IR spectrum) by the Fourier Transfomation method. The mathematical method of Fourier Transformation is just representing the same function but in a different domain, so no information is created or lost. The original function can be obtained by Inverse Fourier Transformation. The Fourier Transform of a function and its inverse are expressed as:

$$F(\omega) = \int_{-\infty}^{\infty} f(x) e^{-2\pi i \omega x} dx. \tag{2}$$

$$f(x) = \int_{-\infty}^{\infty} F(\omega) e^{2\pi i \omega x} d\omega. \tag{3}$$

where f (x) is the time signal and $F(\omega)$ is the frequency signal.

Since a computer can only work with finite discrete signals and not continuous ones, the integral can be replaced by a sum and the infinite borders of the integrals can be replaced by finite numbers [41]:

$$f_k = \frac{1}{N} \Sigma_{n=0}^{N-1} F_n e^{2\pi i k n / N}. \tag{4}$$

$$F_n = \Sigma_{k=0}^{N-1} F_k e^{-2\pi i k n / N}. \tag{5}$$

Figure 8 below, shows the Fourier Transform of an interferogram signal into the frequency space.

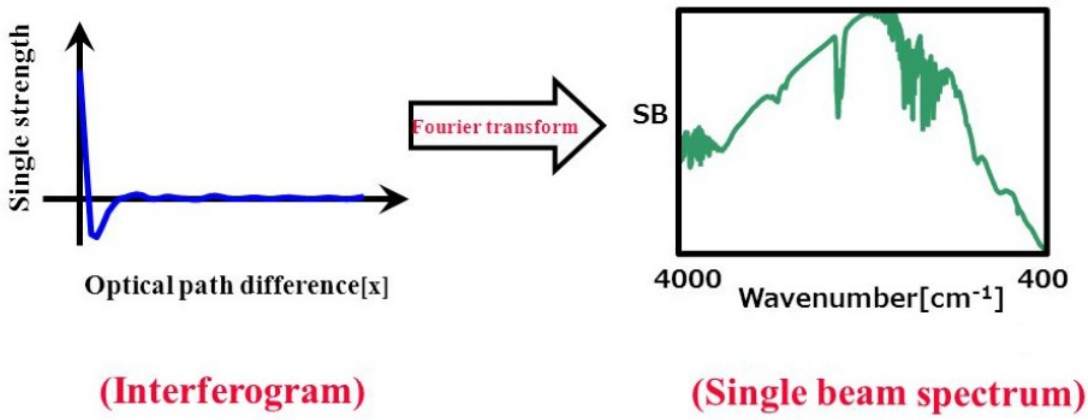

Figure 8: Fourier transform.

The primary advantage of FTIR spectrometer over dispersive IR spectrometer lies in the use of interferometer that results in extremely fast measurements. FTIR spectrometer allows all the frequencies to be measured simultaneously unlike the dispersive one where each frequency is measured individually by the detector.

2. FTIR Reflectivity Measurement

Unpolarized reflectivity measurements were performed in the mid-infrared frequency range from 400 to 4000 cm^{-1} at room temperature at near normal incidence for ZnO pallet samples with 1 cm^{-1} spectral resolution. Parameter adjustment was done using OMNIC software. A gold coated mirror was used to collect a background spectrum before each measurement. This acts as a reference for the measured infrared spectrum where the reflectivity of each sample is compared to that of the coated mirror with an assumed reflectivity 100 %.

3. Kramers-Kronig Method

a. Overview

Many analytic complex functions have been developed in order to relate the real part of that function to an integral containing the imaginary part, and vice versa. The Kramers-Kronig method, named after Ralph Kronig and Hendrik Anthony Kramers, is used to study this relation between the real and imaginary parts of response functions in physical systems. It can be applied to study complex optical functions describing light-matter interaction phenomena, such as susceptibility, the dielectric function, the index of refraction, and reflectivity. The Kramers-Kronig (K-K) relations are used in reflection spectroscopy to describe the relation between the measured reflectance and the phase of the reflectivity [42].

For the K-K relations to be applied, the complex response function $f(\omega) = f_1(\omega) + if_2(\omega)$ must satisfy the following conditions:

1. $f(\omega)$ must be analytic in the upper half of the complex plane, and the poles are below the real axis.

2. The real part $f_1(\omega)$ must be an even function and the imaginary part $f_2(\omega)$ must be odd for real values of ω.

3. The function must vanish at very high frequencies, i.e. the integral of $\frac{f(\omega)}{\omega}$ along a semicircle with infinite radius in the upper half of the complex plane vanishes.

Satisfying these conditions and using the Cauchy residue theorem for complex contour integration, the K-K relations are obtained.

b. Mathematical Derivations

Consider the function $\frac{f(s)}{s-\omega}ds$. This function is analytic in the upper half of the complex plane. By complex analysis, the residue theorem implies that the integral of this function on a closed contour defined by Figure 9 is zero.

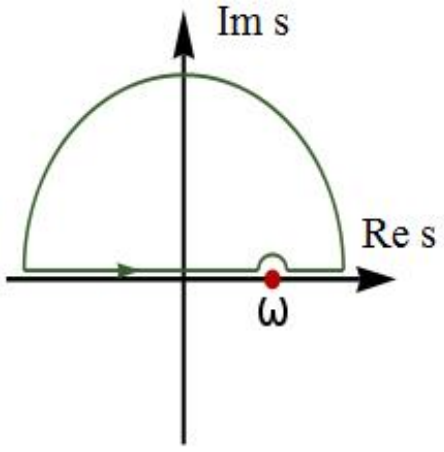

Figure 9: Contour used for deriving the Kramers-Kronig relations

The integral can now be separated into three regions. The first is along the big semicircle which turns out to be equal to zero by the residue theorem. The second region is along the real axis which is given by:

$$P\int_{-\infty}^{\infty}\frac{f(s)}{s-\omega}ds$$

where P is referred to the principle part of the integral.

The third region is along the small semicircle at the pole s = ω which is given by - $i\pi f(\omega)$. This results in the following expression for the integral:

$$\int \frac{f(s)}{s-\omega}ds = P\int_{-\infty}^{\infty} \frac{f(s)}{s-\omega}ds - i\pi f(\omega) = 0 \tag{6}$$

Therefore, the expression of $f(\omega)$ is given by:

$$f(\omega) = \frac{1}{i\pi}P\int_{-\infty}^{\infty} \frac{f(s)}{s-\omega}ds \tag{7}$$

which is the compact form of Kramers-Kronig relations.

Consider a complex function: $\alpha(\omega) = \alpha_1(\omega) + i\alpha_2(\omega)$.

This function $\alpha(\omega)$ satisfies the conditions necessary for K-K relations. Therefore, it can be written as:

$$\alpha = \frac{1}{i\pi}P\int_{-\infty}^{\infty} \frac{\alpha(s)}{s-\omega}ds$$

The function $\alpha(s)$ is also a complex function which takes the form: $\alpha(s) = \alpha_1(s) + i\alpha_2(s)$

Therefore, our equation becomes:

$$\alpha_1(\omega) + i\alpha_2(\omega) = \frac{1}{i\pi}P\int_{-\infty}^{\infty} \frac{\alpha_1(s) + i\alpha_2(s)}{s-\omega}ds$$

$$\implies \alpha_1(\omega) + i\alpha_2(\omega) = \frac{-iP}{\pi}\int_{-\infty}^{\infty} \frac{\alpha_1(s)}{s-\omega}ds + \frac{P}{\pi}\int_{-\infty}^{\infty} \frac{\alpha_2(s)}{s-\omega}ds$$

Taking the real part of each side we get:

$$\alpha_1(\omega) = \frac{P}{\pi}\int_{-\infty}^{\infty} \frac{\alpha_2(s)}{s-\omega}ds$$

Splitting the integral into two parts:

$$\alpha_1(\omega) = \frac{P}{\pi}\int_{-\infty}^{0}\frac{\alpha_2(s)}{s-\omega}ds + \frac{P}{\pi}\int_{0}^{\infty}\frac{\alpha_2(s)}{s-\omega}ds$$

Flipping the first integral and replacing s by -s:

$$\alpha_1(\omega) = \frac{P}{\pi}\left(\int_{0}^{\infty}\frac{\alpha_2(s)}{s+\omega}ds + \int_{0}^{\infty}\frac{\alpha_2(s)}{s-\omega}ds\right)$$

where we have used the second condition that α_2 must be odd: $\alpha_2(-s) = -\alpha_2(s)$

Doing common denominator :

$$\implies \alpha_1(\omega) = \frac{P}{\pi}\left(\int_{0}^{\infty}\frac{\alpha_2(s).(s-\omega) + \alpha_2(s).(s+\omega)}{(s-\omega)(s+\omega)}ds\right)$$

$$\implies \alpha_1(\omega) = \frac{P}{\pi}\left(\int_{0}^{\infty}\frac{\alpha_2(s).2s}{s^2-w^2}ds\right)$$

which finally gives the first relation of Kramers-Kronig:

$$\alpha_1(\omega) = \frac{2.P}{\pi}\int_{0}^{\infty}\frac{s.\alpha_2(s)}{s^2-w^2}ds \tag{8}$$

By similarly taking the imaginary part of each side we get:

$$\alpha_2(\omega) = \frac{-P}{\pi}\int_{-\infty}^{\infty}\frac{\alpha_1(s)}{s-\omega}ds$$

Splitting the integral into two parts, and using the second condition that α_1 must be even: $\alpha_1(-s) = \alpha_1(s)$, we get:

$$\alpha_2(\omega) = \frac{-P}{\pi}\left(\int_{0}^{\infty}\frac{-\alpha_1(s)}{s+\omega} + \int_{0}^{\infty}\frac{\alpha_1(s)}{s-\omega}ds]\right)$$

Which results in the second relation of Kramers-Kronig:

$$\alpha_2(\omega) = \frac{-2.\omega.P}{\pi} \int_0^\infty \frac{\alpha_1(s)}{s^2 - \omega^2} ds \tag{9}$$

Using the K-K relations to analyse our reflectance data, we must be able to relate the amplitude of the reflectance to the phase change between the incident and reflected signal. We first start with the relations:

$$R(\omega) = r(\omega) r^*(\omega) = \rho^2(\omega)$$

$$r(\omega) = \frac{E_{reflected}}{E_{incident}} = \rho(\omega) \exp(i\phi(\omega))$$

where R is the reflectivity, $r(\omega)$ is the Fresnel coefficient of reflectivity, $\rho(\omega)$ is the amplitude, and $\phi(\omega)$ is the phase change.

$$\implies lnr(\omega) = ln\rho(\omega) + i\phi(\omega)$$

where $ln\rho(\omega)$ is α_1 and $\phi(\omega)$ is α_2.

Applying the K-K relation, the phase change can be related to the reflectance by:

$$\phi(\omega) = \frac{-\omega.P}{\pi} \int_0^\infty \frac{lnR(s)}{s^2 - \omega^2} ds \tag{10}$$

which can be written in a more useful form:

$$\phi(\omega) = \frac{-1}{2.\pi} \int_0^\infty ln \mid \frac{s+\omega}{s-\omega} \mid \frac{dlnR(s)}{ds} ds \tag{11}$$

Therefore, once we know the reflectance of a certain material, the phase change can be directly calculated using equation (11). In addition, the optical dielectric function $\varepsilon(\omega)$ with its real and imaginary parts $\varepsilon_1(\omega)$ and $\varepsilon_2(\omega)$ can also be obtained at every frequency

ω using:

$$r(\omega) = \frac{\sqrt{\varepsilon(\omega)} - 1}{\sqrt{\varepsilon(\omega)} + 1} = \frac{n + ik - 1}{n + ik + 1}$$

$$\Longrightarrow \begin{cases} \varepsilon_1(\omega) &= n^2(\omega) - k^2(\omega) \\ \varepsilon_2(\omega) &= 2n(\omega)k(\omega) \end{cases} \tag{12}$$

Thus, the Kramers-Kronig technique permits the determination of these physical quantities from the measured reflectivity data only without the use of any fitting parameters. It is a direct, mathematical method with no physical modeling and assumptions.

As a summary of our work, the reflectivity coefficient can be separated into real and imaginary part r = A + iB where A and B are in terms of the index of refraction n and the extinction coefficient k. Once the measurements are done, they will be extrapolated to the low and high frequency end using Origin software. The results are put in a Kramers-Kronig MATLAB code that gives the values of $\phi(\omega)$ from $R(\omega)$ (Eq. (11)). The values of $\rho(\omega)$ are just the square root of the reflectivity measurements that we have. So we obtain the equation:

$$r(\omega) = \rho(\omega)\exp(i\phi(\omega)) = \rho(\omega)cos(\phi) + i\rho(\omega)sin(\phi)$$

Finally, the two equations are equated as follows:

$$A + iB = \rho cos(\phi) + i\rho sin(\phi)$$

$$\Longrightarrow \begin{cases} A - \rho cos(\phi) &= 0 \\ B - \rho sin(\phi) &= 0 \end{cases} \tag{13}$$

The only unknowns in this system of two equations are the index of refraction and the

extinction coefficient of the bulk material which will be obtained by equating these two equations using a MATLAB code that performs iterations on all the frequency range.

E. Ultraviolet-Visible Reflectance and Analysis

Ultraviolet-Visible spectrometer is an optical characterization technique that uses ultraviolet and visible light to study the electronic transitions between the atomic or molecular energy levels of the sample. Since both ultraviolet and visible radiations have sufficiently high energies they are capable to excite an electron from a lower into higher energy state. Consequently, the UV-VIS spectrometer is also often called ”electronic spectrometer” and it has been proven to be very efficient in calculating the value of the bandgap of the material studied.

1. Experimental Setup

Our UV-VIS experimental measurements were done using the V-570 UV/VIS/NIR Spectrophotometer. It consists of two light sources; a deuterium (D2) lamp (190 to 350 nm) for the UV region and a halogen (W1) lamp (340 to 2500 nm) for the VIS/NIR region. The radiation emitted from the light source reflects off a mirror and is converged into a monochromator where it is dispersed by the grating to generate a monochromated light. The light then paths by a set of mirrors and directed toward the sample or the reference sample or both of them at the same time depending on the type of measurement being accomplished. Finally, the light that has passed through the sample and the reference sample is directed toward the photomultiplier tube or Pbs photoconductive cell to be detected

Since we are interested in measuring the reflectivity spectrum of our samples, we

attached the Absolute Reflectance Measuring Unit (ARMU). This attachment is designed to measure the absolute reflectance of a specular reflecting sample, the relative reflectance of a diffuse reflecting sample as well as the transmittance spectrum of a sample by using the optional solid sample holder for transmittance measurement. ARMU has an integrating sphere and a detector attached to it, in addition to two sample holders; one for the absolute reflectance measurement and the other for the relative reflectance measurements as shown in Figure 9.

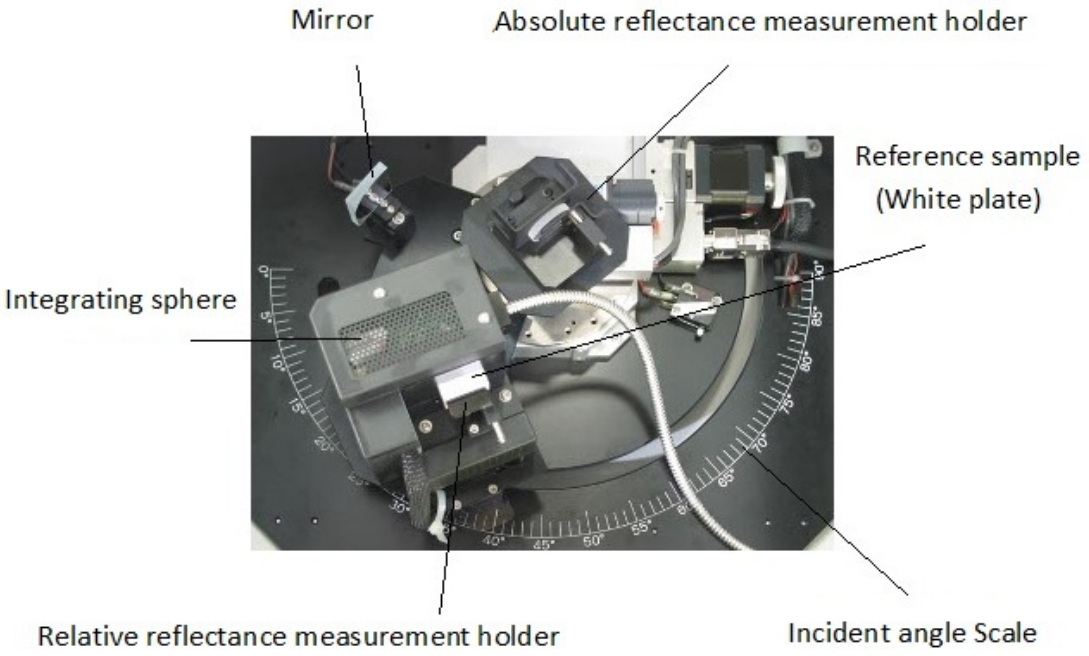

Figure 10: Absolute Reflectance Measuring Unit with its components.

Because our samples undergo diffuse reflectance, the relative reflectance mesurement is required in this case. The device operates by directing the monochromated light toward the reference sample located on the rear of the integrated sphere to which the detector is attached. The reference sample is then replaced by the sample for measuring its spectrum.

2. Operating Procedure

Using the Spectra-Manager software, unpolarized reflectivity were preformed for ZnO pallet samples in the wavelength range 250 to 1800 nm at near normal incidence. Since a little difference in the reflectivity can lead to large variation in the obtained optical properties, a sample holder was designed especially for our samples to integrate the radiation incident on it in order not to lose even 1 % from the absolute value of the reflectivity. The operating procedure followed for UV-VIS measurement is listed below:

1. The standard reflection plate (white plate) is mounted on the relative reflectance measurement holder located on the rear of the integrating sphere.

2. The absolute reflectance measurment holder is removed.

3. The integrating sphere is setted at an incident angle scale 90 degree.

4. Measurement of the baseline correction data is taken.

5. The standard reflection plate is removed and the sample is mounted in place.

6. Measurement of the sample spectrum is taken.

3. Numerical analysis of the measured spectra

We first measure the reflectivity of the whole sample and deduce the effective frequency-dependent amplitude $\rho(\omega)$ and phase $\theta(\omega)$ using Kramers-Kronig theorem. The results obtained from Kramers-Kronig conversion technique constitute our initial guess values for the dielectric properties of the sample under consideration.

In the next step, for each wavelength of the measured spectrum, we give a range of possible values for both refraction index n and extinction coefficient k around the values obtained from Kramers-Kronig. For instance, we take the minimum possible value to be 50% smaller than the value obtained from Kramers-Kronig and the maximum value to be 50% greater than the value obtained from Kramers-Kronig, with an extremely small step,

say 0.001. Then, we take n as a row vector and k as a column vector to form a mesh with cells corresponding to all possible combinations of n and k. In each cell we find the difference between the measured reflectivity and the calculated one using the n and k of the cell. Then, we consider as solution the combination that gives the minimum value, i.e., the minimum difference between calculated and measured reflectivity. In case we obtain more than one solution, we calculate the reflectivity with each potential solution, and we select the one that gives the closest value to the experimentally measured reflectivity. We repeat this procedure for each measured wavelength to plot the spectra of the dielectric properties of the sample under consideration.

CHAPTER IV

RESULTS AND DISCUSSION

In this chapter, we present the experimental results that were obtained and analyzed to characterize the optical properties of ZnO nanoparticles. The structure and morphology of all the samples obtained by XRD and SEM are presented in the first and second sections respectively. In the third section, we present the reflectivity spectra of ZnO nanoparticles prepared by varying the calcination temperature in both UV-VIS and IR regions. In the fourth section, we show the graphs of n, k and ε that were extracted from the Kramers-Kronig method in the IR region. In the last section, we present the optical parameters of the samples as well as the energy loss function in the UV-VIS region that were obtained by using our new numerical technique. Back calculation of the reflectivity spectra to verify the validity of our approach is also presented.

A. XRD Measurements

The X-ray diffraction patterns of all the samples prepared by the processes described above are shown in the figures 11, 12 and 13. These spectra correspond to ZnO nanoparticles prepared by varying zinc nitrate concentration, KOH concentration and calcination temperature, respectively. All the peaks appearing in the XRD patterns are well indexed to the hexagonal ZnO wurtzite structure. No additional diffraction peaks corresponding to impurities are observed within the sensitivity of the measurement.

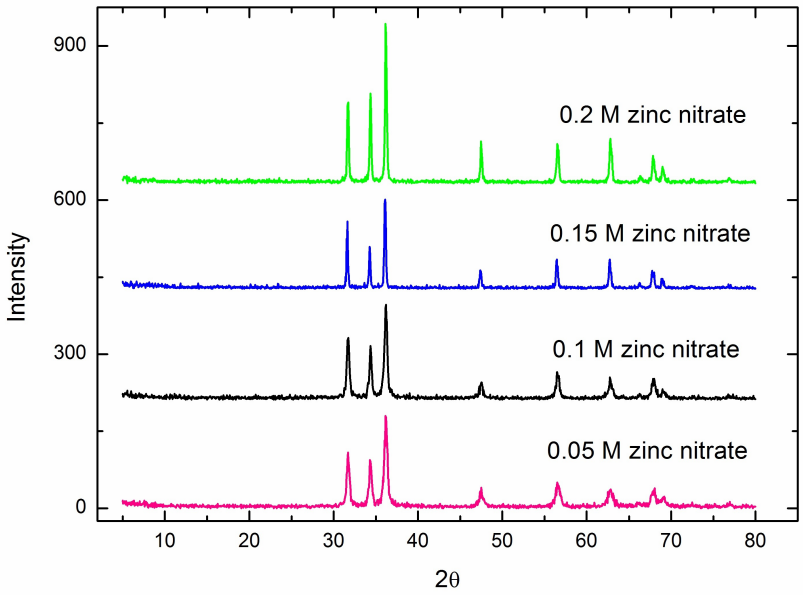

Figure 11: XRD of ZnO samples prepared by varying zinc nitrate concentration and fixing KOH concentration at 0.2 M.

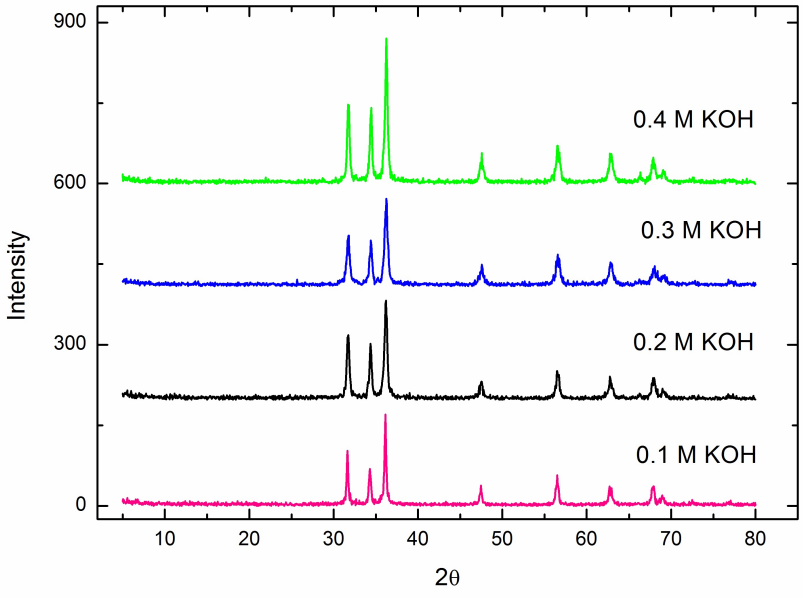

Figure 12: XRD of ZnO samples prepared by varying KOH concentration and fixing $Zn(NO_3)_2.6H_2O$ concentration at 0.1 M.

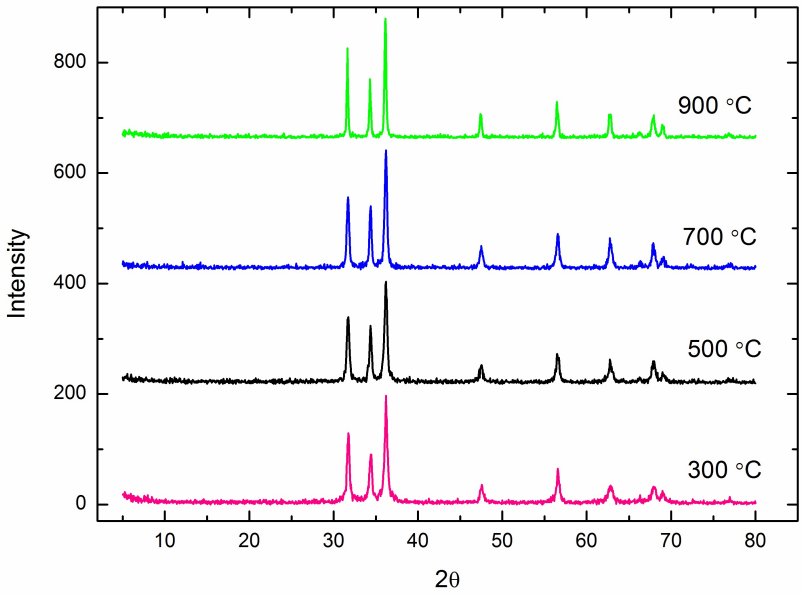

Figure 13: XRD of ZnO samples calcined at different temperatures using 0.1 M $Zn(NO_3)_2.6H_2O$ and 0.2 M KOH concentrations.

B. SEM Images

To determine the best synthesis process that yields to ZnO nanoparticles having uniform size and shape, we characterize our samples by scanning electron microsscope. The SEM images of ZnO nanoparticles prepared with increasing $Zn(NO_3)_2.6H_2O$ concentration are shown in Fig.14. At low conentration of $Zn(NO_3)_2.6H_2O$ (0.05M), we found extensive agglomeration (fusion) of the particles as shown in figure a. With increasing the concentration of $Zn(NO_3)_2.6H_2O$ up to 0.2 M, the SEM images show well defined nanoparticles with small spherical shape as shown in figures b, c and d. However, at 0.2 M $Zn(NO_3)_2.6H_2O$ concentration, we found different sizes of nanoparticles within the same sample as shown in figure d.

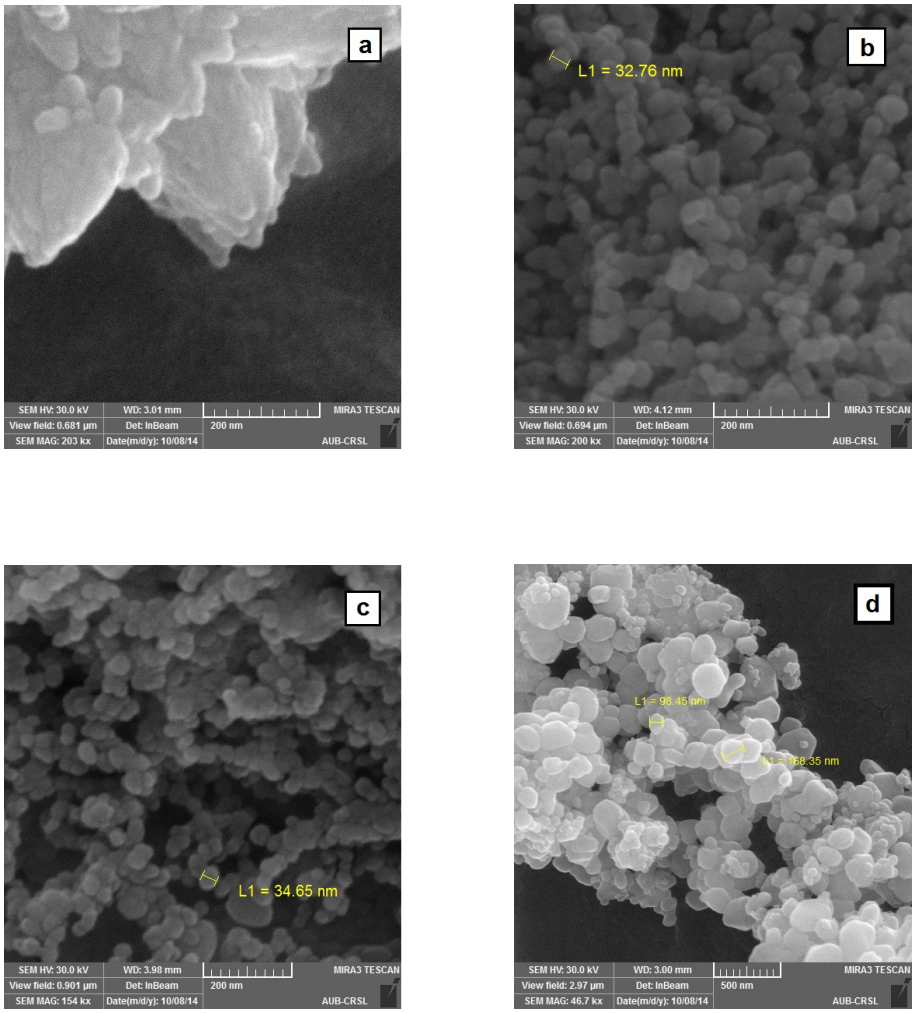

Figure 14: SEM images of ZnO samples prepared with varying $Zn(NO_3)_2.6H_2O$ concentration: (a) 0.05 M, (b) 0.1 M, (c) 0.15 M, (d) 0.2 M and fixing KOH concentration at 0.2 M.

By varying KOH concentration, we observed small spherical shaped nanoparticles with uniform size at 0.1 M and 0.2 M KOH concentrations as shown in Fig.15. However, at 0.3 M and 0.4 M KOH concentrations, we found strong agglomeration in the particles as shown in figures c and d, respectively.

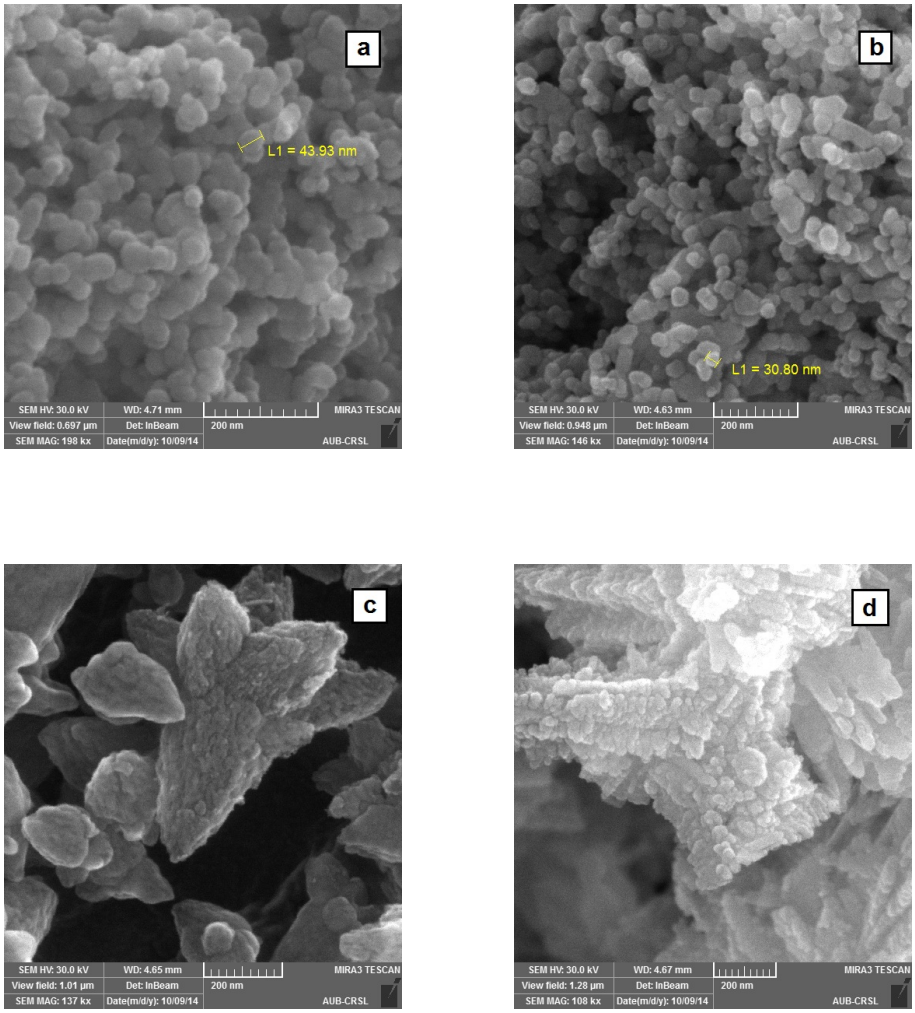

Figure 15: SEM images of ZnO samples prepared with varying KOH concentration: (a) 0.1 M, (b) 0.2 M, (c) 0.3 M, (d) 0.4 M and fixing $Zn(NO_3)_2.6H_2O$ at 0.1 M.

On the other hand, by varying the calcination temperature of the prepared samples, we observed that all the particles prepared by this method well defined have uniform size and shape within the same sample. The average crystallite size was found to increases from 26 nm to 470 nm with increasing the calcination temperature from 300 °C to 900 °C. Such an increase in the particles size is related to the migration of grain boundaries by raising the temperature, causing the coalescence of small grains and formation of large grains [43].

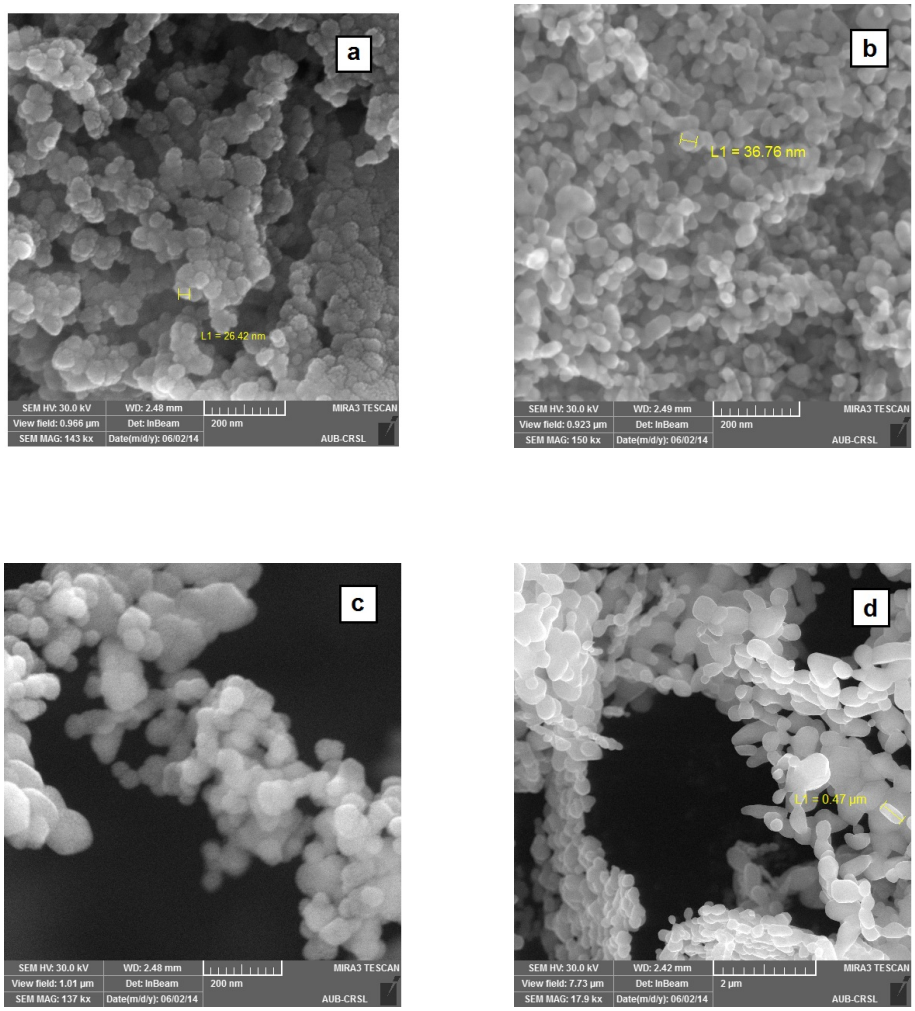

Figure 16: SEM images of ZnO samples calcined at different temperatures: (a) 300 °C, (b) 500 °C, (c) 700 °C, (d) 900 °C using 0.1 M $Zn(NO_3)_2.6H_2O$ and 0.2 M KOH concentrations.

Thus, based on the SEM images, we found that ZnO nanoparticles calcined at different temperatures are the best synthesized samples in terms of the uniformity of their particles size and shape. The crystallite sizes obtained from SEM imaging are shown in table 2.

Table 3: Average crystallite size of ZnO calcined at different temperatures using SEM analysis

Calcination temperature (°C)	Crystallite size (nm)
300	26
500	36
700	75
900	470

C. Reflectivity Measurements

1. IR region

FT-IR reflectance spectra from ZnO nanoparticles prepared by varying the calcination temperature are shown in figure17. The spectra show reflectivity band in the $400cm^{-1}$ to about 600 cm^{-1} spectral range. This band is due to excitation of optical phonons in response to electromagnetic waves. The reflectivity then decreases sharply to reach a minimum value ($R_{min} = 0$) near the longitudinal optical phonon frequency (ω_{LO}). This band is typically known as the reststrahlen band of ZnO. Beyond this region, there is no excitation of optical phonons and thus stabilization in the reflectivity spectra is observed. ZnO sample of 470 nm grain size shows a lower reflectivity band compared to the other samples indicating the presence of defects within the sample, because the defects damp the harmonic oscillators.

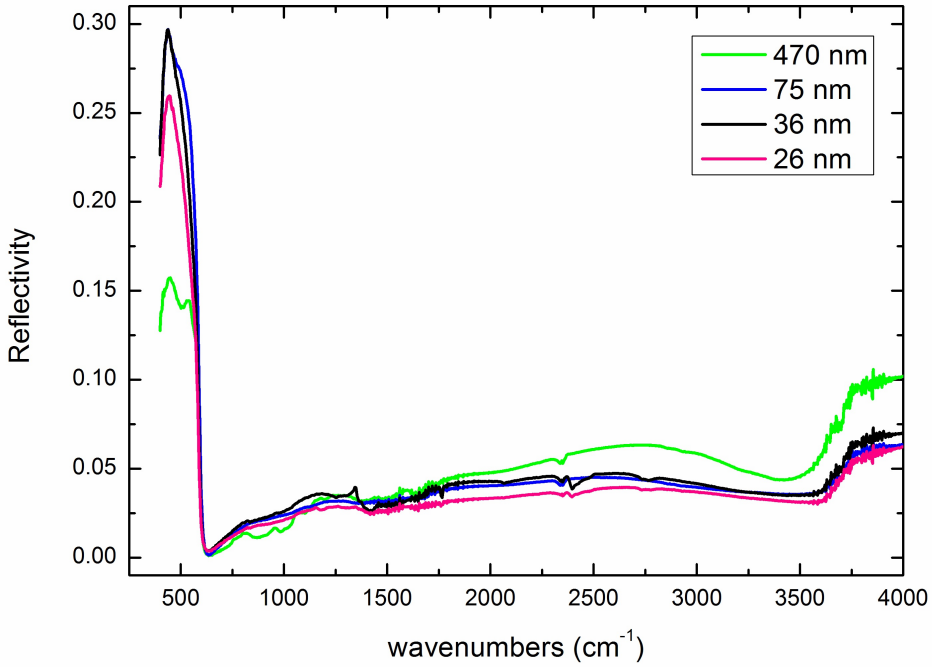

Figure 17: Infrared reflectivity spectra of ZnO nanoparticles calcined at different temperatures: 300 °C, 500 °C, 700 °C and 900 °C using 0.1 M $Zn(NO_3)_2.6H_2O$ and 0.2 M KOH concentrations.

2. UV-VIS region

Figure 18 shows the reflectance spectra from ZnO nanoparticles prepared by varying the calcination temperature in the UV-VIS spectral range. An abrupt change in the reflectance in the 430 nm to 530 nm spectral range is observed for all the samples. This drop in the reflectivity spectra is originated from band-edge absorption of the specimen due to recombination of electron holes in ZnO. Beyond this range, intraband transition results in a decrease in the reflectivity.

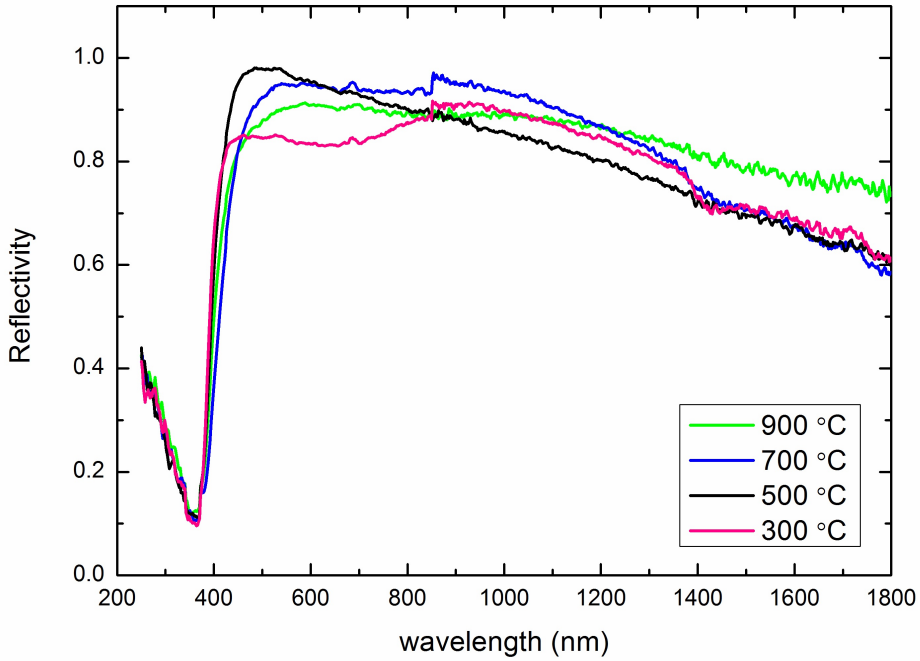

Figure 18: UV-VIS reflectivity spectra of ZnO nanoparticles calcined at different temperatures: 300 °C, 500 °C, 700 °C and 900 °C using 0.1 M $Zn(NO_3)_2.6H_2O$ and 0.2 M KOH concentrations.

D. Determination of optical parameters in IR region

In this section we present the results of Kramers-Kronig method that is used to extract the dielectric properties in mid-IR spectral range.

1. Refraction index (n)

The refraction coefficients of the samples are shown in figure 19 in the 400 cm^{-1} to 4000 cm^{-1} spectral range. The spectra show two phonon resonances at around 410 cm^{-1} and 610 cm^{-1} due to excitation of transverse optical phonons parallel (axial mode) and perpendicular (planar mode) to the c-axis, respectively. A sharp resonance peak is

observed for ZnO sample of 36 nm grain size, which indicates a good crystalline quality. The broad resonance peak for ZnO sample of 470 nm grain size indicates the presence of defects damping the lattice vibrations.

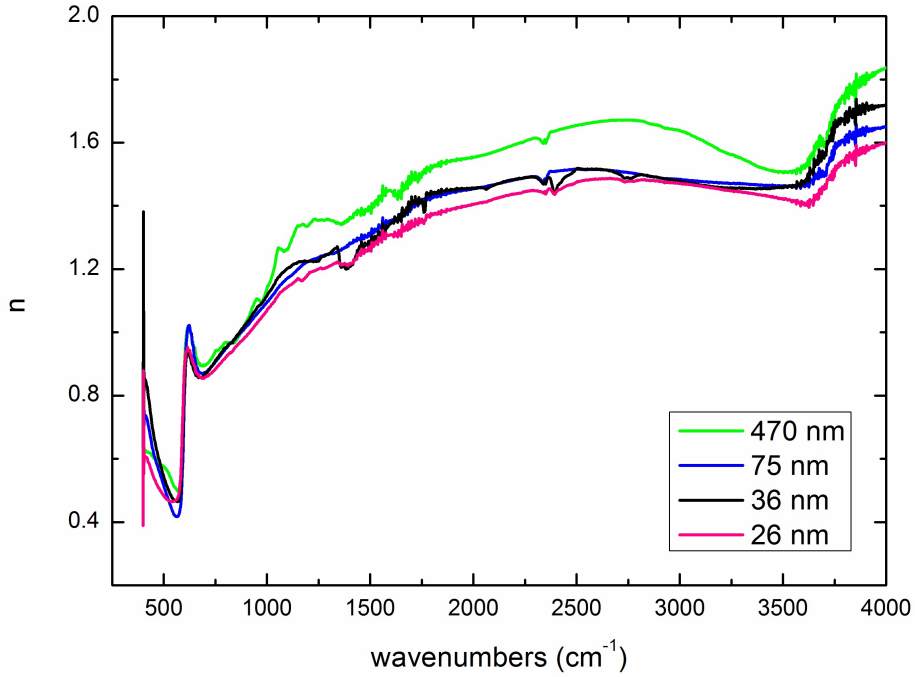

Figure 19: Refractive index of ZnO nanoparticles calcined at different temperatures in the infrared region.

2. *Extinction coefficient (k)*

Fig.20 shows the extinction coefficients of the samples as a function of wavenumber. A peak at around 420 cm^{-1} is observed in all the spectra indicating the absorption of the material at the lattice vibrations frequencies. The intensity of the peak is 0.7969, 1.1353, 1.026, 0.5475 for ZnO nanoparticles of 26 nm, 36 nm, 75 nm and 470 nm respectively.

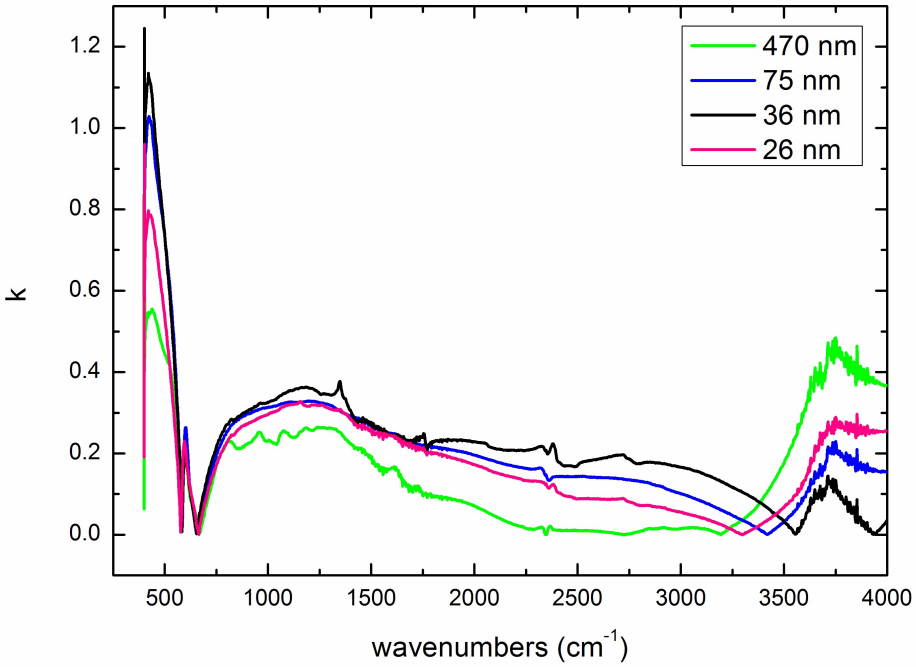

Figure 20: Extinction coefficient of ZnO nanoparticles calcined at different temperatures in the infrared region.

3. Dielectric constant (ε)

The real and imaginary parts of dielectric constant of ZnO in the 400 cm^{-1} to 4000 cm^{-1} spectral range are plotted in figures 21 and 22 respectively. The real part of the dielectric constants ε_1 is negative between transverse optical phonon frequency ω_{TO} and longitudinal optical phonon frequency ω_{LO}. This region corresponds to thermal emission of the sample. The spectra of ε_1 interacts with the zero-axis at the frequency of the longitudinal phonon, that is in the case of ZnO 520 cm^{-1}.

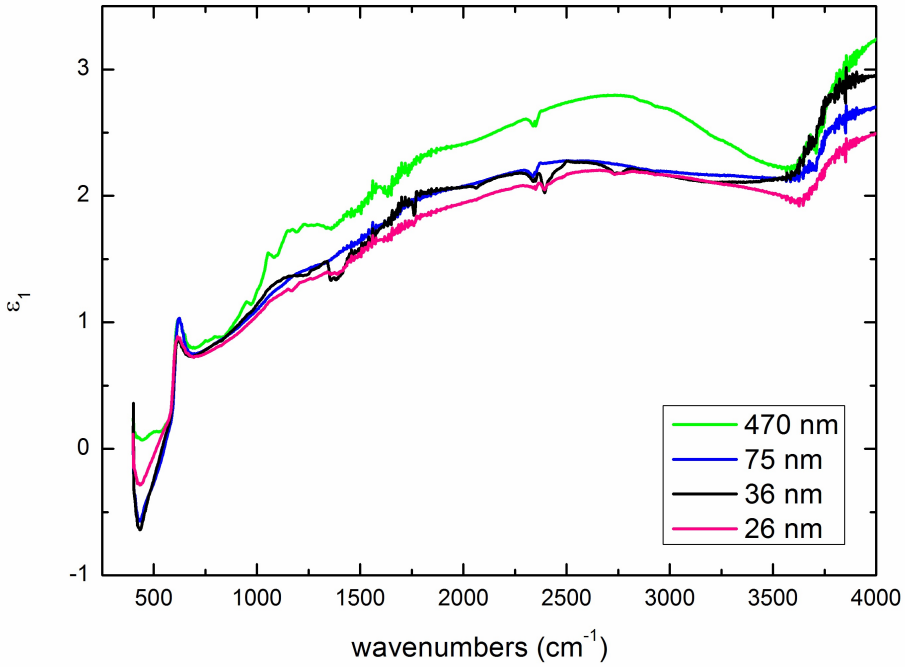

Figure 21: The real parts of dielectric functions of ZnO samples calcined at different temperatures in the infrared region.

The imaginary part ε_2 of the dielectric constant shows two peaks at 420 cm^{-1} and 540 cm^{-1} corresponding to the ω_{TO} along and perpendicular to the material's optical axis.

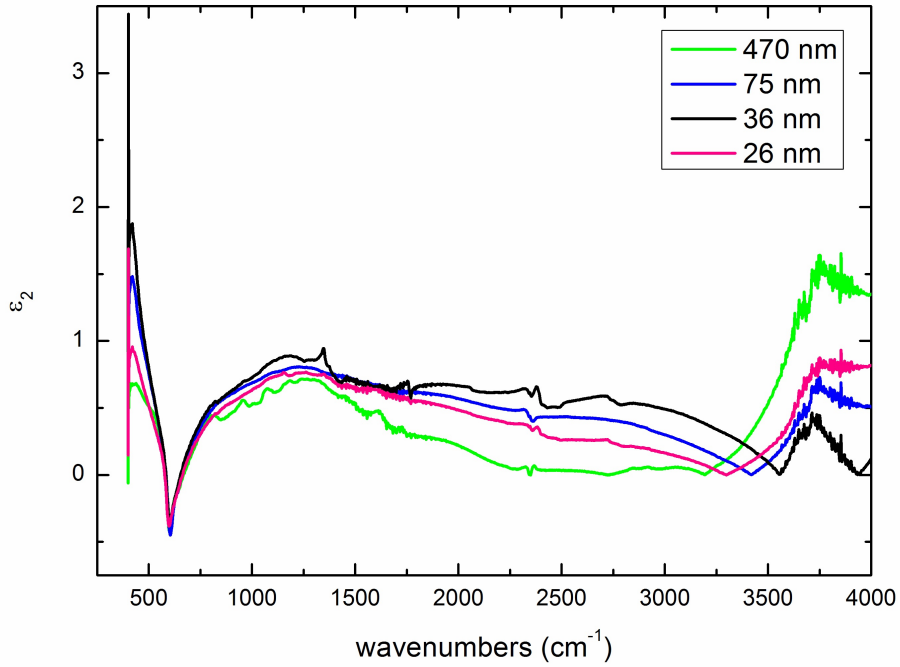

Figure 22: The imaginary parts of dielectric functions of ZnO nanoparticles calcined at different temperatures in the infrared region.

To check the accuracy of the obtained results, back calculation of IR reflectivity spectra was done for all the samples. The results show good agreement between the experimental and calculated spectra as shown in Fig.23, confirming the validity of K-K method in the mid-IR spectral range.

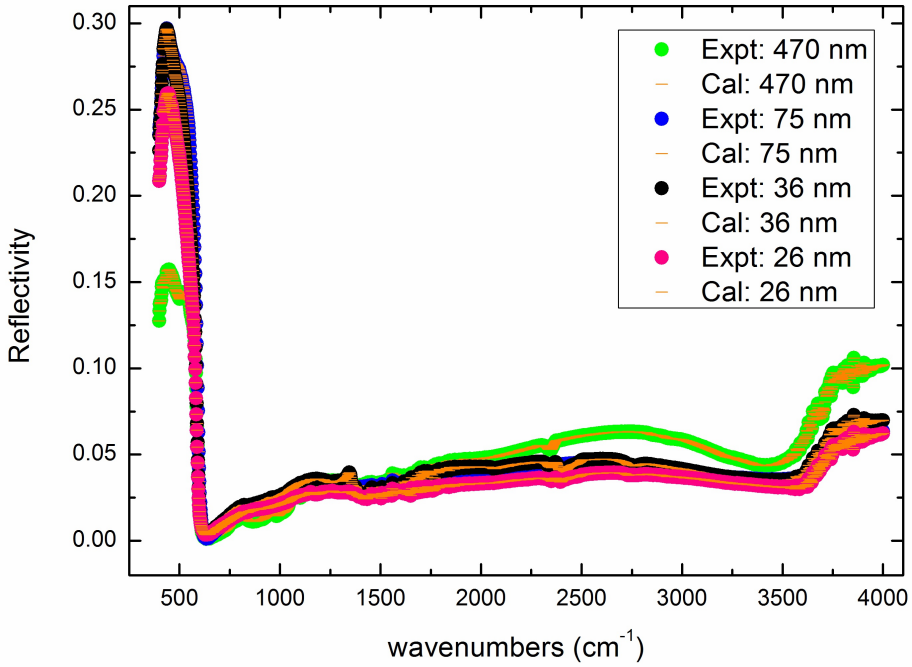

Figure 23: Back calculation of the reflectivity spectra in the IR region.

E. Determination of optical parameters in UV-VIS region

In this section we present the results of our new numerical code that is used to extract the dielectric properties of ZnO: n, k, ε_1, ε_2 and Im $[\varepsilon^{-1}]$ in the UV-VIS spectral range. Backup calculation of UV-VIS reflectivity spectra of the samples is presented to verify the validity of our approach. Comparison between the results obtained from our approach and K-K method is also presented.

1. Refraction index (n)

The refraction coefficients of the samples in the 250 nm - 1800 nm spectral range are shown in Fig.24. The spectra show strong peaks of n(λ) related to resonances of ZnO nanoparticles of 26 nm, 36 nm, 75 nm and 470 nm grain size at 988 nm, 840 nm, 1048

nm, 1164 nm respectively. The shift in the resonance peaks is related to a change in the nature of the defects when the calcination temperature is changed. The increase in the refraction index with λ, before resonance, is associated with anomalous dispersion. After resonance, however, the refraction index tends to decrease with increasing λ; this behavior is associated with normal dispersion.

It is important to see the difference in the refraction index above and below the resonance. On the long wavelength side of the resonance, the refraction index is higher than that on the shorter wavelength side. The difference in the refraction index is due to different polarization mechanisms that come into play at different wavelengths. At wavelengths below resonance, the phase velocity is determined by both electronic and ionic polarizations; however above resonance (at visible wavelengths), ionic polarization is too slow to respond to the electromagnetic field and hence the phase velocity is determined by only electronic polarization. Knowing that the refraction index is defined as n = c/v (where v is the phase velocity), a larger phase velocity results in a lower refraction index. Thus, the refraction index is higher above the resonance [44, 45].

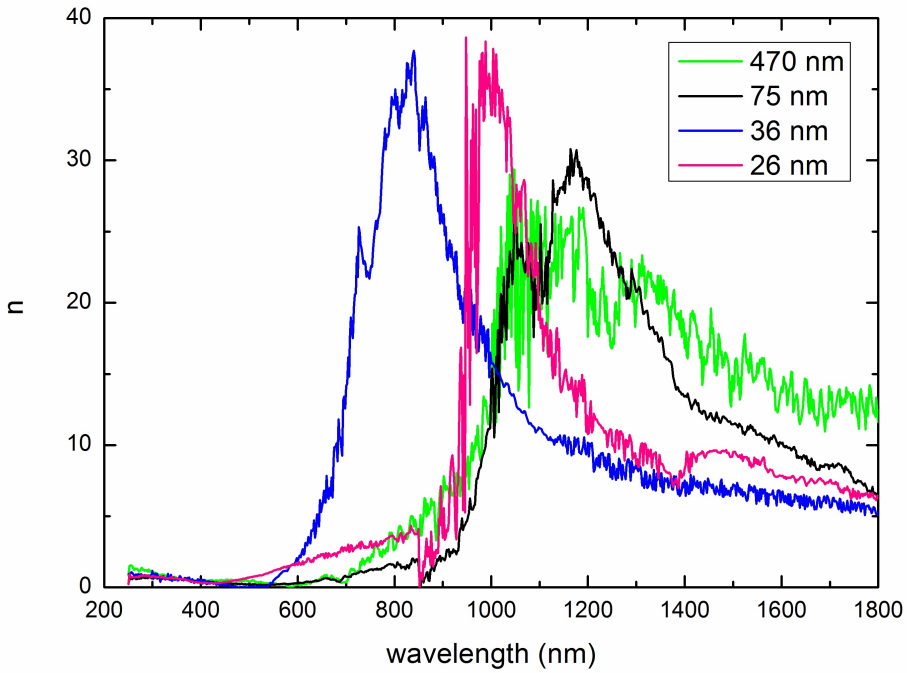

Figure 24: Refractive index of ZnO nanoparticles calcined at different temperatures in the UV-VIS region.

2. Extinction coefficient (k)

Fig.25 shows the extinction coefficients of the samples in the UV-VIS spectral range. The peaks in the extinction coefficients reflects the resonant absorption of energy that occurs in the vicinity of the resonances. It corresponds to the absorption of photons by electrons undergoing electronic transition. A shift in the absorption peak is also noticed, corresponding to a change in the nature of defects complexes when the calcination temperature changes.

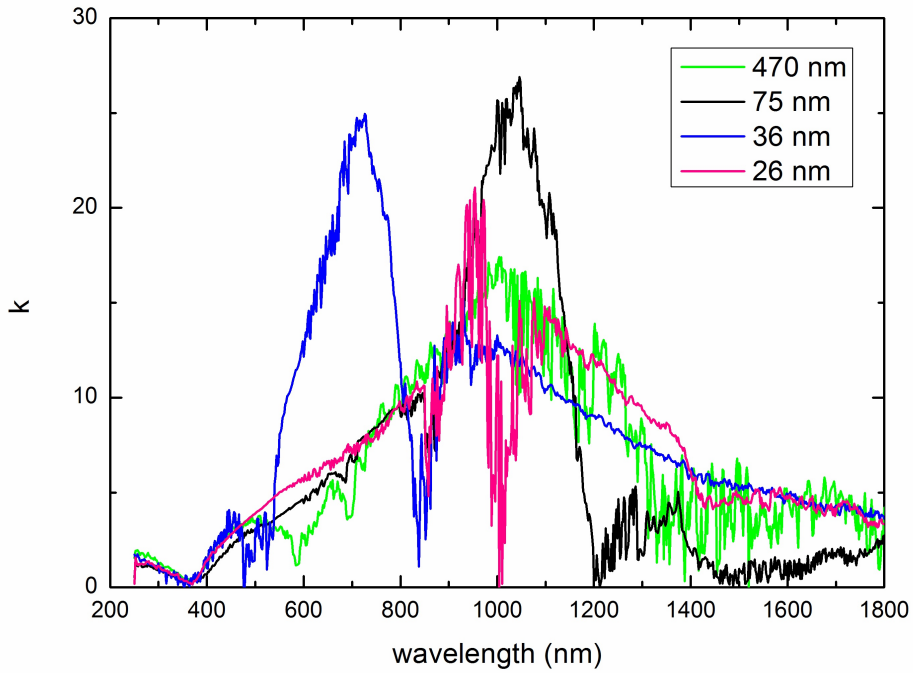

Figure 25: Extinction coefficient of ZnO nanoparticles calcined at different temperatures in the UV-VIS region.

3. Dielectric constant (ε)

The real and imaginary parts of the dielectric constants of the samples in the UV-VIS spectral range are plotted in figures 26 and 27 respectively. It can be noticed that for most wavelengths, when λ is not close to the resonance, ε_1 decreases with increasing λ, and ε_2 is very small due to absorption; this typical behavior is associated with normal dispersion. When λ is very close to resonance, however, the electrons are driven at almost their natural frequency, and resonance occurs. Near resonance, then, ε_1 increases with increasing λ, and ε_2 is no longer small; this behavior is associated with anomalous dispersion. Hence, normal dispersion is seen to occur everywhere except in the neighborhood of a resonance. At a resonating wavelength, the imaginary part of ε is appreciable and the region is called resonant absorption, representing the dissipation of energy from

the EM wave into the medium. As shown in figure 26, the spectra of ε_1 show two resonance peaks for ZnO samples of 26 nm, 36 nm and 75 nm indicating the presence of two valleys in the conduction band. The first resonance peaks that were found to be at 857 nm, 724 nm and 1052 nm are related to the higher valley of the valence band, whereas the second resonance peaks that were observed at 995 nm, 838 nm and 1175 nm are related to the lower valley of the valence band for ZnO nanoparticles of 26 nm, 36 nm and 75 nm, respectively.

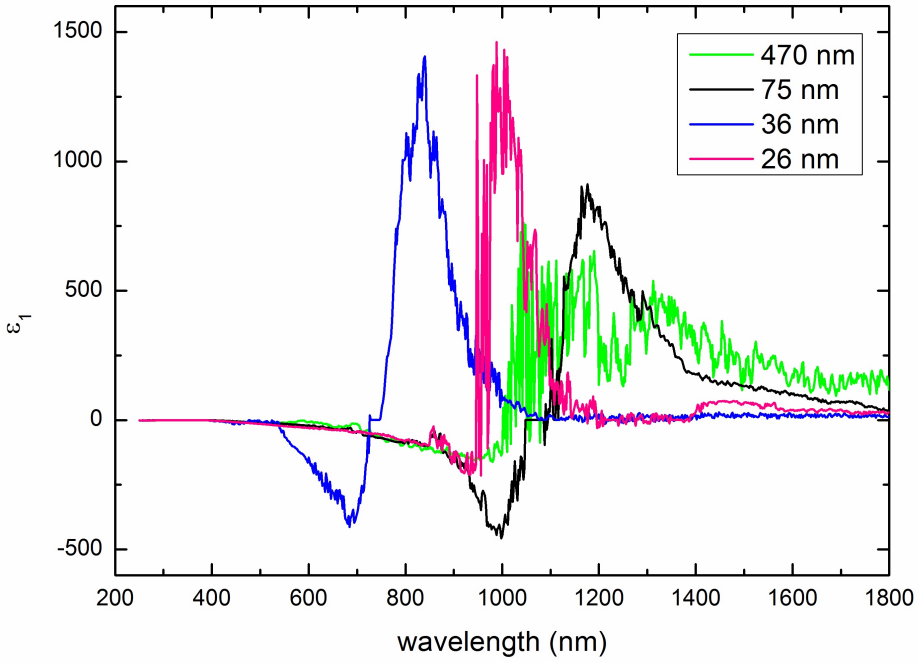

Figure 26: The real parts of dielectric functions of ZnO nanoparticles calcined at different temperatures in the UV-VIS region.

In figure 27, the samples show high imaginary part of the dielectric function ε_2. This indicates the presence of defects within the samples that enhances the material's absorption of light in a wide spectral range, and thus enhances the imaginary part of the dielectric function in a wide spectral range.

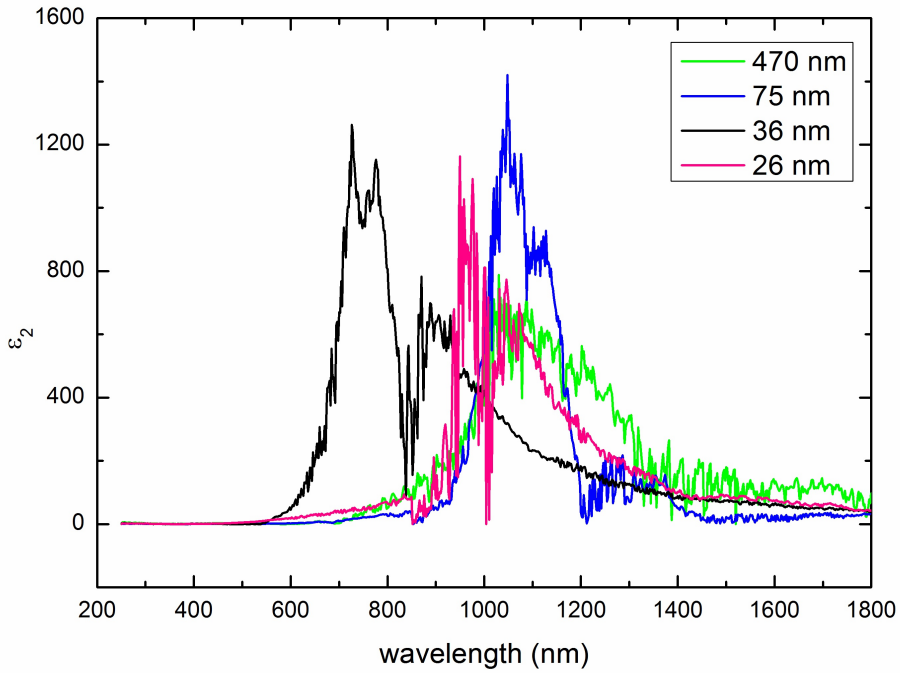

Figure 27: The imaginary parts of dielectric functions of ZnO nanoparticles calcined at different temperatures in the UV-VIS region.

4. Energy loss function

Fig.28 shows the energy loss function of the samples as a function of wavelength. A gap emission is observed at around 371 nm related to transition from the conduction to valence band. A shoulder emisssion is observed at lower wavelengths corresponding to intraband transitions between the excited levels of the conduction band. The emission of the gap of the small grains is so sharp, which indicates a good crystalline quality.

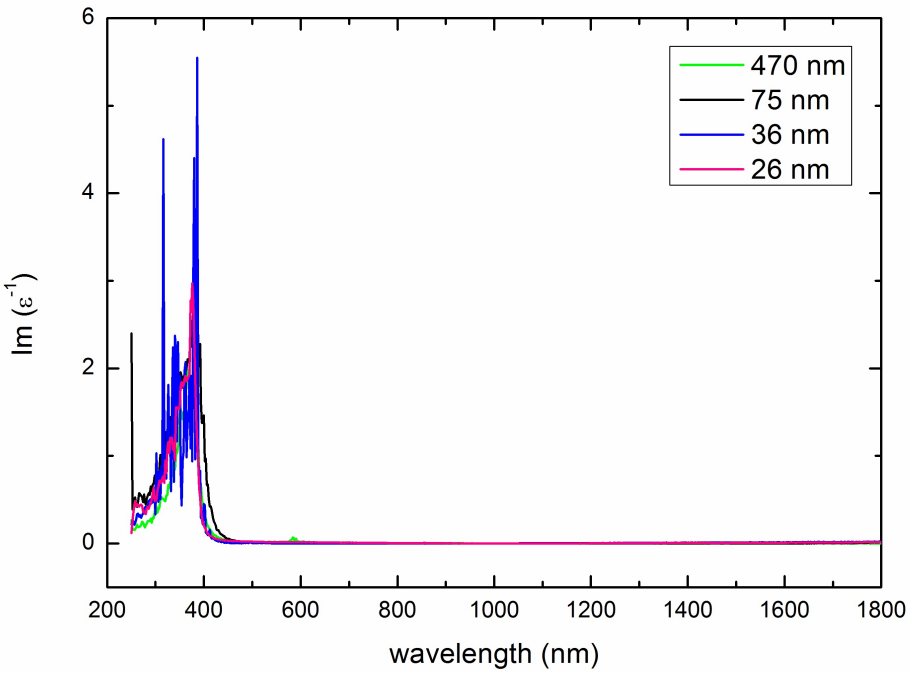

Figure 28: Energy loss functions of ZnO nanoparticles calcined at different temperatures in the UV-VIS region.

Fig.29 shows the semi log plot of the energy loss function as a function of wavelength. Green emission is observed from the sample of 36 nm grain size, and yellow emission is observed from the sample of 470 nm grain size due to interstitial-oxygen (O_i) and oxygen-vacancy (V_o), respectively [46]. Thus, we find that by varying the calcination temperature, the defect complexes change their nature in the host crystal and become radiative.

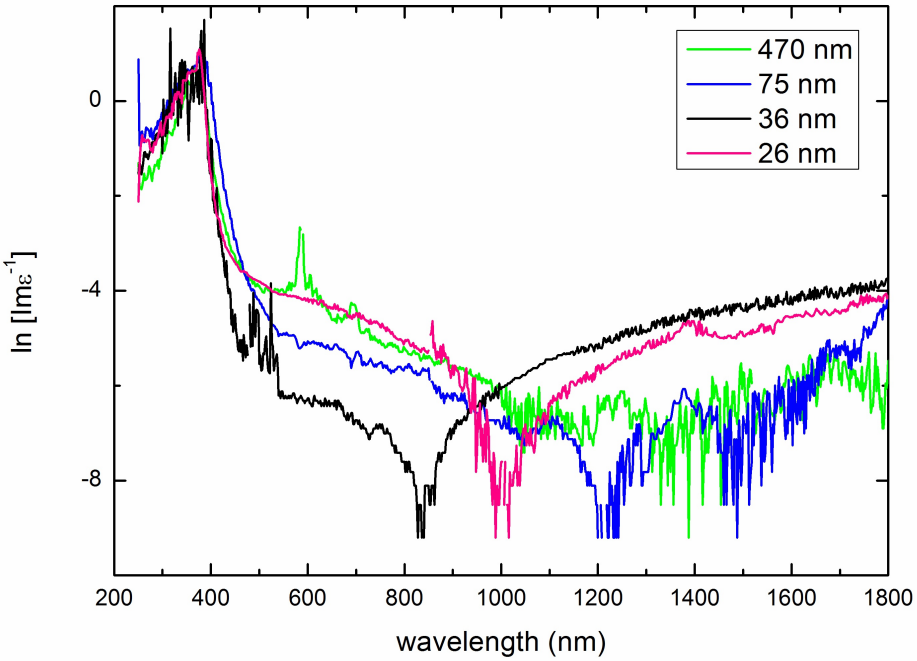

Figure 29: Linear energy loss functions of ZnO nanoparticles calcined at different temperatures in the UV-VIS region.

5. Comparison with K-K method

To verify the reliability of our technique, we back calculated the reflectivity spectra of our samples in the UV-VIS spectral range by using the deduced optical parameters. The results are shown in Fig.30 for ZnO calcined at different temperatures. The calculated reflectivity spectra shows excellent agreement with the measured one, confirming the validity of our developed technique.

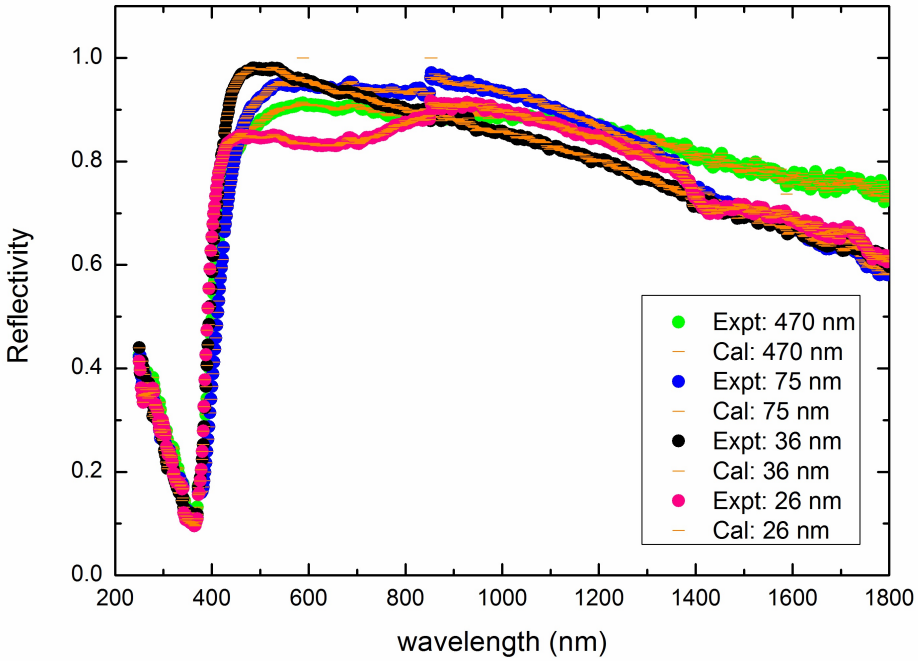

Figure 30: Back calculation of the UV-VIS reflectivity spectra of ZnO nanoparticles using our new numerical technique.

In Fig.31 we present the back calculation of the UV-VIS reflectivity spectra for ZnO nanoparticles of 26 nm grain size using Kramers-Kronig method. Enormous difference between the calculated and measured spectra was found. This clearly demonstrates the accuracy of our developed technique compared to the Kramers-Kronig analysis method in the UV-VIS spectral range.

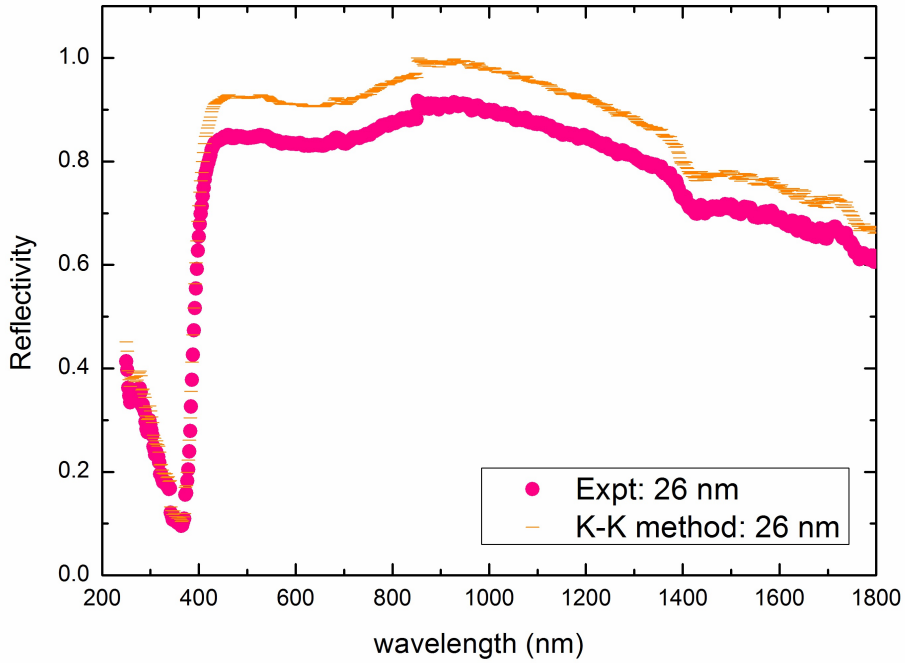

Figure 31: Back calculation of the UV-VIS reflectivity spectrum of ZnO nanoparticles of 26 nm grain size using K-K method.

CHAPTER V

CONCLUSION AND FUTURE WORK

In this thesis, a developed model is achieved to compute the optical parmeters, n and k, of ZnO nanoparticles, at the UV-VIS wavelengths. Infrared optical constants of the prepared samples have been also reported by using Kramers-Kronig method.

ZnO nanoparticles were successfully synthesized via simple precipitation method by controlling different parameters of the precipitation process such as solution concentration and calcination temperature. The structural and morphological properties of these samples were investigated by SEM and XRD analysis. SEM images showed uniformity in the particles size and shape for ZnO nanoparticles calcined at different temperatures compared to the other synthesized samples. The average crystallite size increases with increasing the calcination temperature.

We used UV-VIS and FTIR spectrophotometers to get the reflectivity data of the selected samples. By using Kramers-Kronig method, we then determined n and k with the real and imaginary parts of ε in the IR region. An absorption peak observed at 420 cm^{-1} in the imaginary part of ε corresponds to absorption resonance due to lattice vibrations. A sharp resonance peak in the small grains indicate a good crystalline quality.

K-K method were then combined with our new developed technique to compute the optical parameters in the UV-VIS region. A shift in the absorption peak in the extinction coefficients of the samples was observed due to defects by varying the calcination temperature. The energy loss function showed gap emission at around 371 nm. Green emission was observed from 36 nm grain size ZnO sample and yellow emission was observed from 470 nm grain size ZnO sample.

Finally, to verify the validity of our approach, we back calculated the UV-VIS

reflectivity spectra from the deduced optical parameters, and good agreement was found between the measured and calculated spectra. Back calculation of UV-VIS reflectivity spectrum of 26 nm grain size sample only by using K-K method showed enormous difference between the measured and calculated one. This confirm the importance of our approach in building up a new numerical technique for accurate measurement of the optical parameters at the UV-VIS wavelengths.

The reflectivity based technique described in this work could be applied to study ZnO nanoparticles of smaller sizes reaching the quantum confinement region. A tremendous benefit to nano-scale optoelectronic devices will result from the understanding of size effect on the optical parameters of ZnO.

BIBLIOGRAPHY

[1] Suhana Mohamed Sultan, Peter Ashburn, and Harold MH Chong. Top-down fabrication of zno nwfets. *Advanced Nanoelectronics*, page 331, 2012.

[2] Hadis Morkoç and Ümit Özgür. General properties of zno. *Zinc Oxide: Fundamentals, Materials and Device Technology*, pages 1–76, 2009.

[3] Zhong Lin Wang. Zno nanowire and nanobelt platform for nanotechnology. *Materials Science and Engineering: R: Reports*, 64(3):33–71, 2009.

[4] Chennupati Jagadish and Stephen J Pearton. *Zinc oxide bulk, thin films and nanostructures: processing, properties, and applications*. Elsevier, 2011.

[5] Seung Min Park. Green emission from zno thin films. *Journal of the Korean Physical Society*, 53(1):110–114, 2008.

[6] Xiaotian Yang. Guotong du, xinqiang wang. *Jinzhong Wang, etc. Effect of post-thermal annealing on properties of ZnO thin film grown on c-Al2O3 by metal-organic chemical vapor deposition. Journal of Crystal Growth*, 252(1-3):p275, 2003.

[7] Sayan Bayan and Dambarudhar Mohanta. Defect mediated optical emission of randomly oriented zno nanorods and unusual rectifying behavior of schottky nanojunctions. *Journal of Applied Physics*, 110(5):054316, 2011.

[8] AG Baca, C O'Dwyer, J Brown, D Buckley, P Nam, and A Etcheberry. State-of-the-art program on compound semiconductors 50 (sotapocs 50) and processes at the semiconductor solution interface 3. Electrochemical Society, 2009.

[9] H Kim, A Cepler, C Cetina, D Knies, MS Osofsky, RCY Auyeung, and A PiquÚ. Pulsed laser deposition of zr–n codoped p-type zno thin films. *Applied Physics A*, 93(3):593–598, 2008.

[10] Andreas Waag. Electrical conductivity and doping. In *Zinc Oxide*, pages 95–119. Springer, 2010.

[11] Rahul Srivastava. *ZnO Nanostructure Based Dye Sensitized Solar Cell*. PhD thesis, 2012.

[12] O Madelung, U Rössler, and M Shultz. Ii–vi and i–vii compounds; semimagnetic compounds, 1999.

[13] Sadao Adachi. *Properties of semiconductor alloys: group-IV, III-V and II-VI semiconductors*, volume 28. John Wiley & Sons, 2009.

[14] Diana I Florescu, LG Mourokh, Fred H Pollak, David C Look, G Cantwell, and X Li. High spatial resolution thermal conductivity of bulk zno (0001). *Journal of applied physics*, 91(2):890–892, 2002.

[15] Mintang Liu. *Synthesis of ZnO nanowires and applications as gas sensors*. PhD thesis, University of Saskatchewan, 2010.

[16] Karuppannan Rokesh, Alagarsamy Pandikumar, and Kandasamy Jothivenkatachalam. Zinc oxide nanopillar: Preparation, characterization and its photoelectrocatalytic activity. *Materials Focus*, 3(5):345–349, 2014.

[17] Erich Mollwo. Thermal emission of zinc oxide crystals. *Z. angew. Phys*, 6:257, 1954.

[18] WL Bond. Measurement of the refractive indices of several crystals. *Journal of Applied Physics*, 36(5):1674–1677, 1965.

[19] YS Park and JR Schneider. Index of refraction of zno. *Journal of Applied Physics*, 39(7):3049–3052, 1968.

[20] RL Hengehold, RJ Almassy, and FL Pedrotti. Electron energy-loss and ultraviolet-reflectivity spectra of crystalline zno. *Physical Review B*, 1(12):4784, 1970.

[21] R Klucker, H Nelkowski, YS Park, M Skibowski, and TS Wagner. Optical anisotropy of zno in the ultraviolet region. *physica status solidi (b)*, 45(1):265–272, 1971.

[22] WS Hu, ZG Liu, J Sun, SN Zhu, QQ Xu, D Feng, and ZM Ji. Optical properties of pulsed laser deposited zno thin films. *Journal of Physics and Chemistry of Solids*, 58(6):853–857, 1997.

[23] XW Sun and HS Kwok. Optical properties of epitaxially grown zinc oxide films on sapphire by pulsed laser deposition. *Journal of Applied Physics*, 86(1):408–411, 1999.

[24] Hisashi Yoshikawa and Sadao Adachi. Optical constants of zno. *Japanese Journal of Applied Physics*, 36(10R):6237, 1997.

[25] GE Jellison, LA Boatner, et al. Optical functions of uniaxial zno determined by generalized ellipsometry. *Physical Review B*, 58(7):3586, 1998.

[26] N Ashkenov, BN Mbenkum, C Bundesmann, V Riede, M Lorenz, D Spemann, EM Kaidashev, A Kasic, M Schubert, M Grundmann, et al. Infrared dielectric functions and phonon modes of high-quality zno films. *Journal of applied physics*, 93(1):126–133, 2003.

[27] Ebru Şenadım, Sıtkı Eker, Hamide Kavak, and Ramazan Esen. Optical and structural parameters of the zno thin film grown by pulsed filtered cathodic vacuum arc deposition. *Solid state communications*, 139(9):479–484, 2006.

[28] SW Xue, XT Zu, WL Zhou, HX Deng, X Xiang, L Zhang, and H Deng. Effects of post-thermal annealing on the optical constants of zno thin film. *Journal of Alloys and Compounds*, 448(1):21–26, 2008.

[29] Jiaguang Han, Wei Chen, Jun Zhang, Mingxia He, Abul K Azad, S Ray, Y Zhao, and Weili Zhang. Terahertz response of bulk and nanostructured zno. *Session 1P4 Terahertz Optoelectronics*, page 135, 2008.

[30] A Schleife, C Rödl, F Fuchs, J Furthmüller, and F Bechstedt. Optical and energy-loss spectra of mgo, zno, and cdo from ab initio many-body calculations. *Physical Review B*, 80(3):035112, 2009.

[31] Mujdat Caglar, Saliha Ilican, and Yasemin Caglar. Influence of dopant concentration on the optical properties of zno: In films by sol–gel method. *Thin Solid Films*, 517(17):5023–5028, 2009.

[32] M Ebrahimizadeh Abrishami, SM Hosseini, E Attaran Kakhki, A Kompany, and M Ghasemifard. Synthesis and structure of pure and mn-doped zinc oxide nanopowders. *International Journal of Nanoscience*, 9(01n02):19–28, 2010.

[33] Pohkok Ooi, Saicheong Lee, Shashiong Ng, Zainuriah Hassan, and Haslan Abu Hassan. Far infrared optical properties of bulk wurtzite zinc oxide semiconductor. *Journal of Materials Science & Technology*, 27(5):465–470, 2011.

[34] Z Serbetçi, HM El-Nasser, and Fahrettin Yakuphanoglu. Photoluminescence and refractive index dispersion properties of zno nanofibers grown by sol–gel method. *Spectrochimica Acta Part A: Molecular and Biomolecular Spectroscopy*, 86:405–409, 2012.

[35] D-T Phan, AAM Farag, F Yakuphanoglu, and GS Chung. Optical and photoluminescence properties of ga doped zno nanostructures by sol-gel method. *Journal of electroceramics*, 29(1):12–22, 2012.

[36] Saliha Ilican. Effect of na doping on the microstructures and optical properties of zno nanorods. *Journal of Alloys and Compounds*, 553:225–232, 2013.

[37] JM Khoshman, JN Hilfiker, N Tabet, and ME Kordesch. Multiple oscillator models for the optical constants of polycrystalline zinc oxide thin films over a wide wavelength range. *Applied Surface Science*, 307:558–565, 2014.

[38] Reza Zamiri, Avito Rebelo, Golriz Zamiri, Atena Adnani, Ajay Kuashal, Michael Scott Belsley, and JMF Ferreira. Far-infrared optical constants of zno and zno/ag nanostructures. *RSC Advances*, 4(40):20902–20908, 2014.

[39] Darick J. Baker. *Surface modification and characterization of zinc oxide for use in organic photovoltaic devices*. PhD thesis, Colorado School of Mines, 2011.

[40] Sajjad Hussain. Investigation of structural and optical properties of nanocrystalline zno. 2008.

[41] Mirvat Shams Eddine. Optical analysis of boron nitride thin films. Master's thesis, American University of Beirut, 2012.

[42] N. Rahbany, M. Kazan, M. Tabbal, R. Tauk, J. Jabbour, J. Brault, B. Damilano, and J. Massies. Measurement of the effect of plasmon gas oscillation on the dielectric properties of p-and n-doped alxga1- xn films using infrared spectroscopy. *Journal of Applied Physics*, 114, 2013.

[43] Surabhi Siva Kumar, Putcha Venkateswarlu, Vanka Ranga Rao, and Gollapalli Nagewsara Rao. Synthesis, characterization and optical properties of zinc oxide nanoparticles. *International Nano Letters*, 3(1):1–6, 2013.

[44] Paul Harrison. *Quantum wells, wires and dots: theoretical and computational physics of semiconductor nanostructures*. John Wiley & Sons, 2005.

[45] John S McCloy. Methods for prediction of refractive index in glasses for the infrared. In *SPIE Defense, Security, and Sensing*, pages 80160G–80160G. International Society for Optics and Photonics, 2011.

[46] S Yamauchi, Y Goto, and T Hariu. Photoluminescence studies of undoped and nitrogen-doped zno layers grown by plasma-assisted epitaxy. *Journal of crystal growth*, 260(1):1–6, 2004.